Investigation of turbulent transport regimes in the tokamak edge by using two-fluid simulations

M. Giacomin [1],† and P. Ricci[1]

[1]Ecole Polytechnique Fédérale de Lausanne (EPFL), Swiss Plasma Center (SPC), CH-1015 Lausanne, Switzerland

The results of flux-driven, two-fluid simulations in single-null configurations are used to investigate the processes determining the turbulent transport in the tokamak edge. Three turbulent transport regimes are identified: (i) a developed transport regime with turbulence driven by an interchange instability, which shares a number of features with the standard L-mode of tokamak operation; (ii) a suppressed transport regime, characterized by a higher value of the energy confinement time, low-amplitude relative fluctuations driven by a Kelvin–Helmholtz instability, a strong $E \times B$ sheared flow and the formation of a transport barrier, which recalls the H-mode; and (iii) a degraded confinement regime, characterized by a catastrophically large interchange-driven turbulent transport, which recalls the crossing of the Greenwald density limit. We derive an analytical expression of the pressure gradient length in the three regimes. The transition from the developed transport regime to the suppressed transport regime is obtained by increasing the heat source or decreasing the collisionality and vice versa for the transition from the developed transport regime to the degraded confinement regime. An analytical expression of the power threshold to access the suppressed transport regime, linked to the power threshold for H-mode access, as well as the maximum density achievable before entering the degraded confinement regime, related to the Greenwald density, are also derived. The experimental dependencies of the power threshold for H-mode access on density, tokamak major radius and isotope mass are retrieved. The analytical estimate of the density limit contains the correct dependence on the plasma current and on the tokamak minor radius.

Key words: fusion plasma, plasma simulation, plasma dynamics

1. Introduction

The turbulent plasma dynamics in the edge plays a key role in determining the overall performances of a tokamak by governing its confinement properties. Indeed, fundamental phenomena, such as the L–H transition (Wagner *et al.* 1982) and the density limit (Greenwald *et al.* 1988; Greenwald 2002), strongly depend on the plasma dynamics in the tokamak edge. Because of the persisting uncertainties in the fundamental understanding of these phenomena, the design of future fusion devices is based on scaling laws.

A scaling law for the power threshold for the L–H transition, P_{LH}, has been proposed by Martin, Takizuka & the ITPA CDBM H-mode Threshold Database Working Group (2008)

† Email address for correspondence: maurizio.giacomin@epfl.ch

based on an international H-mode threshold power database:

$$P_{\mathrm{LH}} \propto n_e^{0.78 \pm 0.04} B_T^{0.77 \pm 0.03} a^{0.98 \pm 0.08} R^{1.0 \pm 0.1}, \tag{1.1}$$

where n_e is the line-averaged electron density, B_T is the toroidal magnetic field at the tokamak axis, a is the tokamak minor radius and R is the tokamak major radius. In addition, it has been experimentally observed that P_{LH} in a single-null geometry is lower when the ion-∇B drift direction is towards the X-point, rather than away from it (ASDEX Team 1989) and that P_{LH} depends inversely on m_i/m_e (Righi *et al.* 1999; Maggi *et al.* 2017). Experimental observations in Alcator C-Mod (Snipes *et al.* 1996) and DIII-D (Thomas *et al.* 1998) tokamaks have pointed out the presence of hysteresis in the L–H transition, although this is not a feature universally observed (Ryter *et al.* 2013). Furthermore, just before the L–H transition, experimentally observed is the formation at the tokamak edge of a clear well in the radial electric field profile that induces a strong $\boldsymbol{E} \times \boldsymbol{B}$ shear flow, which, in turn, suppresses plasma turbulence (Groebner, Burrell & Seraydarian 1990; Burrell 1997; Ryter *et al.* 2015). While several models have attempted to uncover the mechanism behind the L–H transition, there is no theory that accounts for all the observations (Connor & Wilson 2000).

The density limit represents the maximum plasma density achievable in tokamaks before the plasma develops a strong magnetohydrodynamic activity that leads to the degradation of particle confinement or even a disruption. An experimental scaling law for the density limit, denoted as Greenwald density n_{G}, has been derived by Greenwald *et al.* (1988):

$$n_{\mathrm{G}} = \frac{I_p}{\pi a^2}, \tag{1.2}$$

where I_p is the plasma current in MA, a is the tokamak minor radius in m and n_{G} is the line-averaged density in 10^{20} m^{-3}. Experimental observations show that the cooling of the plasma edge is a key element that characterizes the density limit (Vershkov & Mirnov 1974; Fielding *et al.* 1977). In fact, experimental studies reveal that the density limit can be exceeded by operating with peaked density profiles (Kamada *et al.* 1991; Mahdavi *et al.* 2002; Valovic *et al.* 2002; Lang *et al.* 2012), thus providing a strong evidence of the link between the density limit and edge physics (Greenwald 2002). It has been experimentally observed by Hong *et al.* (2017) that, when the line-averaged density approaches the density limit, the edge shear flow collapses and, consequently, the turbulent transport strongly increases near the separatrix. While there is no widely accepted first-principles model for the density limit, research in this area has focused on mechanisms which lead to strong edge cooling, in particular on the effect of the plasma collisionality on enhanced turbulent transport (Greenwald 2002).

The first attempts to provide a unified theoretical description of turbulent transport in the tokamak edge that includes the L-mode confinement regime, the H-mode confinement regime and a degraded confinement regime, related to the crossing of the density limit, are discussed by Scott (1997) and Rogers, Drake & Zeiler (1998) in a circular and sheared geometry, based on fluid flux-tube simulations. The transitions from the L-mode to the H-mode and from the L-mode to the density limit are observed by changing the value of the plasma collisionality and β. The dependence of edge transport on these parameters was then experimentally observed by LaBombard *et al.* (2005). A more recent work (Hajjar, Diamond & Malkov 2018) based on the Hasegawa–Wakatani model (Hasegawa & Wakatani 1983) in the low-β limit shows that both the dynamics that characterizes the L–H transition and the density limit can be described as the result of varying the plasma collisionality. By changing the collisionality, three different regimes

are identified: a low-confinement regime, a high-confinement regime and a regime of degraded particle confinement, which is associated with the density limit.

The goal of the present paper is to extend previous investigations of the edge turbulent regimes by considering a more realistic geometry, i.e. a lower single-null configuration, while retaining the coupling between the edge and both the core and the scrape-off layer (SOL), as a crucial element in determining the plasma dynamics at the tokamak edge. In fact, the transport mechanisms occurring in the tokamak periphery are expected to result from a complex interplay among core, edge and SOL physics (Fichtmüller, Corrigan & Simonini 1998; Dif-pradalier *et al.* 2017; Grenfell *et al.* 2019), which is difficult to properly model with a simulation domain that does not include all of them. As a consequence, we perform turbulence simulations of the whole tokamak in order to approach this interplay.

Turbulence in the tokamak core is most often simulated by means of gyrokinetic codes, while fluid codes are usually applied in the SOL, taking advantage of its higher plasma collisionality. This separation undermines the possibilities to advance our understanding of the plasma dynamics in the tokamak edge. For this reason, recently, significant effort has been made in order to extend gyrokinetic models towards the edge and the SOL (Qin *et al.* 2007; Hahm, Wang & Madsen 2009; Frei, Jorge & Ricci 2020). The first gyrokinetic simulation of the L–H transition that encompasses the edge and the SOL was carried out using the XGC1 code (Chang *et al.* 2017; Ku *et al.* 2018). Since the computational cost of a gyrokinetic simulation of the L–H transition on a global transport time scale remains prohibitively high (Chang *et al.* 2017), an ion heat flux at the edge was imposed in the XGC1 L–H simulation, considerably larger than the experimental one. This large flux allowed a reduced computational cost of the simulation, as the L–H transition was due to fast electrostatic bifurcation occurring on a time scale considerably shorter than the one required to reach the global steady-state transport conditions. Other efforts to extend gyrokinetic codes to simulate turbulence in open-field-line systems include the Gkeyll (Shi *et al.* 2017), GENE (Pan *et al.* 2018), ELMFIRE (Chôné *et al.* 2018) and COGENT (Dorf & Dorr 2020) codes. In this paper, we follow a different approach and we extend fluid simulations to the core region, in order to cover the whole tokamak plasma volume. While not providing an accurate description of turbulence in the core, these simulations allow us to explore the parameter space of edge turbulence at different values of heat source and plasma collisionality in a global transport steady state that is the result of the heat and particle sources in the core, turbulent transport and the losses at the vessel. Using these simulations, we draw a portrait of the edge turbulent regimes that can be used as a basis to interpret the results of more complete kinetic simulations.

Our study is based on simulations carried out with GBS (Ricci *et al.* 2012; Halpern *et al.* 2016; Paruta *et al.* 2018), a three-dimensional, flux-driven, two-fluid simulation code that has been developed to study plasma turbulence in the tokamak boundary. Similarly to other turbulent codes, such as BOUT++ (Dudson *et al.* 2015), GDB (Zhu, Francisquez & Rogers 2018), GRILLIX (Stegmeir *et al.* 2018), HESEL (Nielsen *et al.* 2015) and TOKAM3X (Tamain *et al.* 2016), GBS evolves the drift-reduced Braginskii's equations (Zeiler, Drake & Rogers 1997), a set of two-fluid equations valid for describing phenomena occurring on time scales longer than $1/\Omega_{ci}$, with $\Omega_{ci} = eB_T/m_i$ the ion cyclotron frequency, perpendicular length scales longer than the ion Larmor radius and parallel length scales longer than the mean free path.

Early fluid simulations performed with the BOUT code have already shown that the physics of the L–H transition can be addressed by means of fluid models (Xu *et al.* 2000, 2002), even though fluid models exclude a large fraction of modes that are relevant to edge transport, e.g. trapped electron modes, electron temperature gradients, microtearing modes and kinetic ballooning modes, while retaining the fluid limit of the ion temperature

gradient modes (Mosetto *et al.* 2015). Later numerical investigations of the L–H transition have been carried out using two- and three-dimensional fluid simulations and have pointed out the spontaneous formation of a transport barrier (Rasmussen *et al.* 2015; Chôné *et al.* 2014, 2015). Indeed, despite their simplicity, our simulations show the presence of three turbulent transport regimes: (i) a developed transport regime, which we associate with the standard L-mode; (ii) a suppressed transport regime, characterized by a higher value of the energy confinement time due to the onset of a transport barrier near the separatrix, and a lower relative fluctuation level, with features that recall the H-mode; and (iii) a degraded confinement regime, characterized by a catastrophically large turbulent transport, which we link to the density limit. In the developed transport regime and degraded confinement regime, turbulent transport is driven by the interchange instability, while in the suppressed transport regime it is driven by the Kelvin–Helmholtz (KH) instability. We then analyse the transitions between these regimes. As the heat source increases, a transition from the developed transport regime to the suppressed transport regime is observed. This transition is due to the formation of a strong $E \times B$ shear across the separatrix, which stabilizes the interchange instability and destabilizes the KH instability. At the transition, a transport barrier forms at the tokamak edge and, consequently, the energy confinement time increases by a factor of approximately two. In fact, the transition from the developed transport regime to the suppressed transport regime shows common features to the L–H transition observed in experiments. By imposing a flux balance at the separatrix between perpendicular and parallel transport, we then derive an equation for the heat source threshold, which can be identified as the power threshold for H-mode access, that we compare to the experimental scaling law of (1.1). The transition from the developed transport regime to the degraded confinement regime is obtained by increasing the normalized plasma collisionality, proportional to the plasma density, or by reducing the heat source. We derive an analytical estimate of the maximum density achievable before accessing the degraded confinement regime. The estimate is compared to the Greenwald density limit of (1.2).

The paper is organized as follows. In § 2, we describe the physical model considered to study turbulent transport in the tokamak edge. An overview of simulation results is presented in § 3, where we discuss the observation of three turbulent transport regimes. In § 4, we derive the analytical expressions of the equilibrium pressure gradient length in the three transport regimes. The heat source threshold to access the suppressed transport regime and the density threshold to access the degraded confinement regime are derived in § 5. The conclusions follow in § 6.

2. Simulation model

Our investigations are based on a drift-reduced Braginskii two-fluid plasma model implemented in the GBS code (Ricci *et al.* 2012; Halpern *et al.* 2016; Paruta *et al.* 2018). The application of drift-reduced fluid models to the study of plasma turbulence is valid when the electron mean-free path is shorter than the parallel connection length, $\lambda_e \ll L_\parallel \sim 2\pi q R$, and the dominant modes develop on perpendicular scale lengths larger than the ion Larmor radius, $k_\perp \rho_i \ll 1$. The high collisionality required by fluid models is typically observed in the edge of L-mode discharges. Regarding the H-mode, we note that, for typical values of density and temperature at the top of the pedestal for neutral beam heated discharges of a medium size tokamak such as TCV, $\lambda_e/L_\parallel$ ranges from 0.05 ($T_e \simeq$ 100 eV and $n \simeq 5 \times 10^{19}$ m^{-3}) to 0.4 ($T_e \simeq$ 200 eV and $n \simeq 3 \times 10^{19}$ m^{-3}), depending on the external gas injection rate (Sheikh *et al.* 2018), thus providing a justification for the use of a fluid model. On the other hand, in the case of JET tokamak, typical values of density and temperature at the top of the pedestal (Beurskens *et al.* 2011) ($T_e \simeq$ 900 eV

and $n \simeq 7 \times 10^{19}$ m^{-3}) lead to $\lambda_e/L_\parallel \simeq 80$. Focusing on the drift approximation that, contrary to more advanced fluid models (e.g. Wiesenberger *et al.* 2019), does not allow us to describe finite Larmor radius effects, we observe that the dominant modes in our simulations satisfy $k_\perp \rho_i \ll 1$, consistent with our model hypothesis, although turbulence in the tokamak edge can also be driven by unstable modes with $k_\perp \rho_i \sim 1$ (Jenko & Dorland 2001; Dickinson *et al.* 2012).

For the sake of simplicity, we consider a rather simple drift-reduced Braginskii two-fluid model for this first exploration of the parameter space. For instance, we consider the electrostatic limit, even if electromagnetic effects are important for the edge turbulent transport in H-mode (e.g. Wan *et al.* 2013; Doerk *et al.* 2015; Kriete *et al.* 2020), by playing a role in constraining the pedestal height and width (e.g. Snyder *et al.* 2004, 2009) and by affecting the SOL dynamics at high β (e.g. Halpern *et al.* 2013*b*). The use of the electrostatic limit is motivated by Hajjar *et al.* (2018), which shows that, even in the low-β limit, different turbulent regimes can be retrieved by varying the plasma collisionality. We also use the Boussinesq approximation in the evaluation of the polarization current (Yu, Krasheninnikov & Guzdar 2006; Ricci *et al.* 2012). The effect of the Boussinesq approximation is discussed in Yu *et al.* (2006) and Bodi *et al.* (2011), showing that it has a negligible effect on SOL turbulence. In the edge, the validity of the Boussinesq approximation is addressed in Stegmeir *et al.* (2019) and Ross *et al.* (2019) showing that there is no substantial difference in the equilibrium profiles when the Boussinesq approximation is considered. Although in theoretical (Chôné *et al.* 2014, 2015) and experimental (Viezzer *et al.* 2013) works it is shown that neoclassical corrections can play an important role in the onset of transport barriers and, consequently, in the L–H transition, we do not include these effects in our model. Trapped particle modes, which can also play an important role in the L–H transition, especially in low-aspect-ratio devices (Rewoldt *et al.* 1996; Dannert & Jenko 2005), are neglected here. Finally, while the neutral dynamics may also have an effect on the L–H transition dynamics, as shown by Shaing & Hsu (1995), Carreras, Diamond & Vetoulis (1996) and Owen *et al.* (1998), we do not include the interplay between plasma and neutrals, although this is implemented in GBS (Wersal & Ricci 2015). Within these approximations, the model equations we consider are the following:

$$\frac{\partial n}{\partial t} = -\frac{\rho_*^{-1}}{B}[\phi, n] + \frac{2}{B}[C(p_e) - nC(\phi)] - \nabla_\parallel(nv_{\parallel e}) + D_n \nabla_\perp^2 n + s_n, \qquad (2.1)$$

$$\frac{\partial \omega}{\partial t} = -\frac{\rho_*^{-1}}{B}[\phi, \omega] - v_{\parallel i}\nabla_\parallel \omega + \frac{B^2}{n}\nabla_\parallel j_\parallel + \frac{2B}{n}C(p_e + \tau p_i) + \frac{B}{3n}C(G_i) + D_\omega \nabla_\perp^2 \omega, \qquad (2.2)$$

$$\frac{\partial v_{\parallel e}}{\partial t} = -\frac{\rho_*^{-1}}{B}[\phi, v_{\parallel e}] - v_{\parallel e}\nabla_\parallel v_{\parallel e} + \frac{m_i}{m_e}\left(\nu j_\parallel + \nabla_\parallel \phi - \frac{1}{n}\nabla_\parallel p_e - 0.71\nabla_\parallel T_e\right)$$
$$+ \frac{4}{3n}\frac{m_i}{m_e}\eta_{0,e}\nabla_\parallel^2 v_{\parallel e} + D_{v_{\parallel e}}\nabla_\perp^2 v_{\parallel e}, \qquad (2.3)$$

$$\frac{\partial v_{\parallel i}}{\partial t} = -\frac{\rho_*^{-1}}{B}[\phi, v_{\parallel i}] - v_{\parallel i}\nabla_\parallel v_{\parallel i} - \frac{1}{n}\nabla_\parallel(p_e + \tau p_i) + \frac{4}{3n}\eta_{0,i}\nabla_\parallel^2 v_{\parallel i} + D_{v_{\parallel i}}\nabla_\perp^2 v_{\parallel i}, \qquad (2.4)$$

$$\frac{\partial T_e}{\partial t} = -\frac{\rho_*^{-1}}{B}[\phi, T_e] - v_{\|e}\nabla_\| T_e + \frac{2}{3}T_e\left[0.71\nabla_\| v_{\|i} - 1.71\nabla_\| v_{\|e} + 0.71(v_{\|i} - v_{\|e})\frac{\nabla_\| n}{n}\right]$$

$$+ \frac{4}{3}\frac{T_e}{B}\left[\frac{7}{2}C(T_e) + \frac{T_e}{n}C(n) - C(\phi)\right] + \chi_{\perp e}\nabla_\perp^2 T_e + \chi_{\|e}\nabla_\|^2 T_e + s_{T_e}, \tag{2.5}$$

$$\frac{\partial T_i}{\partial t} = -\frac{\rho_*^{-1}}{B}[\phi, T_i] - v_{\|i}\nabla_\| T_i + \frac{4}{3}\frac{T_i}{B}\left[C(T_e) + \frac{T_e}{n}C(n) - C(\phi)\right] - \frac{10}{3}\tau\frac{T_i}{B}C(T_i)$$

$$+ \frac{2}{3}T_i(v_{\|i} - v_{\|e})\frac{\nabla_\| n}{n} - \frac{2}{3}T_i\nabla_\| v_{\|e} + \chi_{\perp i}\nabla_\perp^2 T_i + \chi_{\|i}\nabla_\|^2 T_i + s_{T_i}, \tag{2.6}$$

$$\nabla_\perp^2 \phi = \omega - \tau\nabla_\perp^2 T_i. \tag{2.7}$$

In (2.1)–(2.7) and in the following (unless specified otherwise), the density, n, the electron temperature, T_e, and the ion temperature, T_i, are normalized to the reference values n_0, T_{e0} and T_{i0}. The electron and ion parallel velocities, $v_{\|e}$ and $v_{\|i}$, are normalized to the reference sound speed $c_{s0} = \sqrt{T_{e0}/m_i}$. The norm of the magnetic field, B, is normalized to the reference value B_T, which, under the assumption of large aspect ratio (Jolliet *et al.* 2014; Paruta *et al.* 2018), is assumed to be constant. Perpendicular lengths are normalized to the ion sound Larmor radius $\rho_{s0} = c_{s0}/\Omega_{ci}$ and parallel lengths are normalized to the tokamak major radius R_0. Time is normalized to R_0/c_{s0}. The dimensionless parameters appearing in the model equations are the normalized ion sound Larmor radius, $\rho_* = \rho_{s0}/R_0$, the ion to electron temperature ratio, $\tau = T_{i0}/T_{e0}$, the normalized electron and ion viscosities, $\eta_{0,e}$ and $\eta_{0,i}$, the normalized electron parallel and perpendicular thermal conductivities, $\chi_{\|e}$ and $\chi_{\perp e}$, the corresponding ion quantities, $\chi_{\|i}$ and $\chi_{\perp i}$, and the normalized Spitzer resistivity, $\nu = e^2 n_0 R_0/(m_i c_{s0}\sigma_\|) = \nu_0 T_e^{-3/2}$, with

$$\sigma_\| = \left(1.96\frac{n_0 e^2\tau_e}{m_e}\right) n = \left(\frac{5.88}{4\sqrt{2\pi}}\frac{(4\pi\epsilon_0)^2}{e^2}\frac{T_{e0}^{3/2}}{\lambda\sqrt{m_e}}\right)T_e^{3/2}, \tag{2.8}$$

$$\nu_0 = \frac{4\sqrt{2\pi}}{5.88}\frac{e^4}{(4\pi\epsilon_0)^2}\frac{\sqrt{m_e}R_0 n_0\lambda}{m_i c_{s0}T_{e0}^{3/2}}, \tag{2.9}$$

where λ is the Coulomb logarithm. We highlight that the normalized Spitzer resistivity depends linearly on the reference density n_0. The numerical diffusion terms, $D_f\nabla_\perp^2 f$, are added for numerical stability and they lead to significantly smaller transport than the turbulent processes described by the simulations. By considering typical values at the separatrix of a TCV L-mode discharge (tokamak major radius $R_0 \simeq 0.9$ m and toroidal magnetic field at the tokamak axis $B_T \simeq 1.4$ T) as reference density and electron temperature, i.e. $n_0 \simeq 10^{19}$ m^{-3} and $T_{e0} \simeq 20$ eV, we obtain a reference value for the numerical perpendicular diffusion coefficient of the order of 10^{-2} m^2 s^{-1}, two orders of magnitude smaller than the effective diffusion coefficient due to turbulence. The source terms in the density and temperature equations, s_n and s_T, are added to fuel and heat the plasma.

The spatial operators appearing in (2.1)–(2.7) are the $E \times B$ convective term $[g, f] = \boldsymbol{b} \cdot (\nabla g \times \nabla f)$, the curvature operator $C(f) = B/2[\nabla \times (\boldsymbol{b}/B)] \cdot \nabla f$, the parallel gradient $\nabla_\| f = \boldsymbol{b} \cdot \nabla f$ and the perpendicular Laplacian $\nabla_\perp^2 f = \nabla \cdot [(\boldsymbol{b} \times \nabla f) \times \boldsymbol{b}]$, where

$b = B/B$ is the unit vector of the magnetic field. The toroidally symmetric equilibrium magnetic field is written in terms of the poloidal magnetic flux ψ, normalized to $\rho_{s0}^2 B_T$, as

$$B = \pm \nabla \varphi + \rho_* \nabla \psi \times \nabla \varphi, \tag{2.10}$$

where φ is the toroidal angle, with $\nabla \varphi$ normalized to R_0. The plus (minus) sign refers to the direction of the toroidal magnetic field with the ion-∇B drift pointing upwards (downwards). The poloidal magnetic flux is a function of the normalized tokamak major radius R and of the vertical coordinate Z, i.e. $\psi = \psi(R, Z)$. Under the assumption of large aspect ratio, $\epsilon = a/R_0 \ll 1$, and poloidal magnetic field much smaller than the toroidal one, $\delta = \rho_* \|\nabla \psi\| \ll 1$, we can compute the differential operators appearing in (2.1)–(2.7) by retaining only the zeroth-order terms in ϵ and δ. In (R, φ, Z) toroidal coordinates, the curvature operator in dimensionless units can be expanded as

$$C(f) = \frac{\rho_*^{-1}}{2B} \left(\frac{B_\varphi}{B^2} \partial_Z B^2 \partial_R f - \frac{B_\varphi}{B^2} \partial_R B^2 \partial_Z f \right) + O(\epsilon, \delta), \tag{2.11}$$

where $B_\varphi = B_T R_0 / R$. These terms take into account the spatial variation of B^2. Since

$$B^2 = B_T^2 \left(\frac{R_0^2}{R^2} + O(\delta^2) \right), \tag{2.12}$$

its spatial derivatives at zeroth order in ϵ and δ are

$$\partial_Z B^2 = 0, \tag{2.13}$$

$$\partial_R B^2 = -2\rho_* B_T^2. \tag{2.14}$$

Finally, the curvature operator at zeroth order in ϵ and δ becomes

$$C(f) = \pm \partial_Z f + O(\epsilon, \delta). \tag{2.15}$$

Similar algebra leads to the other differential operators at zeroth order in ϵ and δ (see Paruta *et al.* (2018) for details). In summary, the differential operators implemented in GBS in (R, φ, Z) toroidal coordinates are

$$[\phi, f] = \pm \left(\frac{\partial \phi}{\partial Z} \frac{\partial f}{\partial R} - \frac{\partial \phi}{\partial R} \frac{\partial f}{\partial Z} \right), \tag{2.16}$$

$$C(f) = \pm \frac{\partial f}{\partial Z}, \tag{2.17}$$

$$\nabla_\parallel f = \frac{\partial \psi}{\partial Z} \frac{\partial f}{\partial R} - \frac{\partial \psi}{\partial R} \frac{\partial f}{\partial Z} \pm \frac{\partial f}{\partial \varphi}, \tag{2.18}$$

$$\nabla_\perp^2 f = \frac{\partial^2 f}{\partial R^2} + \frac{\partial^2 f}{\partial Z^2}, \tag{2.19}$$

$$\nabla_\parallel^2 f = \nabla_\parallel (\nabla_\parallel f), \tag{2.20}$$

where the plus (minus) sign is again used for the ion-∇B drift pointing upwards (downwards). For the analysis of the turbulent transport in §4, flux coordinates $(\nabla \psi, \nabla \chi, \nabla \varphi)$ are considered, where $\nabla \psi$ denotes the direction orthogonal to flux surfaces, $\nabla \varphi$ is the toroidal direction and $\nabla \chi = \nabla \varphi \times \nabla \psi$.
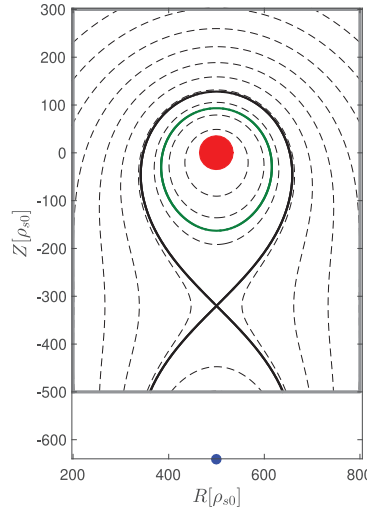
FIGURE 1. Contour plot of the poloidal flux function ψ considered in the present work (black dashed line). The separatrix is shown as a solid black line. The boundary domain is indicated by a solid grey line. The red circle represents the plasma current, while the blue circle, located outside the domain, represents the current filament used to generate the X-point. The flux surface $\psi = \psi_n = \psi_T$ is shown as a solid green line.

Similarly to the simulations presented in Giacomin, Stenger & Ricci (2020), we consider (2.1)–(2.7) in a rectangular poloidal cross-section of size L_R and L_Z in the radial and vertical directions, respectively. The single-null magnetic configuration used in the simulations presented herein is analytically obtained by solving the Biot–Savart law for a straight current filament, which is located outside the domain, and a current density with Gaussian profile, which is centred at the tokamak magnetic axis, (R_0, Z_0), and mimics the plasma current (see figure 1). The current filament and the plasma current are centred at the same radial position.

The density and the temperature sources are analytical and toroidally uniform functions of $\psi(R, Z)$:

$$s_n = s_{n0} \exp\left(-\frac{(\psi(R, Z) - \psi_n)^2}{\Delta_n^2}\right), \tag{2.21}$$

$$s_T = \frac{s_{T0}}{2}\left[\tanh\left(-\frac{\psi(R, Z) - \psi_T}{\Delta_T}\right) + 1\right], \tag{2.22}$$

where ψ_n and ψ_T, displayed in figure 1, are flux surfaces located inside the last closed flux surface (LCFS). The density source is localized around the flux surface ψ_n, close to the separatrix, and mimics the ionization process, while the temperature source extends through the entire core and mimics the ohmic heating. We define S_n and S_T as the total density and temperature source integrated over the area inside the separatrix:

$$S_n = \int_{A_{\mathrm{LCFS}}} \rho_* s_n(R, Z) \, \mathrm{d}R \, \mathrm{d}Z \tag{2.23}$$

and

$$S_T = \int_{A_{\mathrm{LCFS}}} \rho_* s_T(R, Z) \, \mathrm{d}R \, \mathrm{d}Z, \tag{2.24}$$

where the factor ρ_* appears from the normalization. Analogously, we define the electron power source $S_p = \int_{A_{LCFS}} \rho_* s_p \, \mathrm{d}R \, \mathrm{d}Z$, with $s_p = n s_{T_e} + T_e s_n$ and s_{T_e} the electron temperature source.

Magnetic pre-sheath boundary conditions, derived by Loizu *et al.* (2012), are applied at the target plates. Neglecting correction terms linked to radial derivatives of the density and potential at the target plate, these boundary conditions can be expressed as

$$v_{\|i} = \pm\sqrt{T_e + \tau T_i}, \tag{2.25}$$

$$v_{\|e} = \pm\sqrt{T_e + \tau T_i} \, \max\left\{\exp\left(\Lambda - \frac{\phi}{T_e}\right), \exp\left(\Lambda\right)\right\}, \tag{2.26}$$

$$\partial_Z n = \mp \frac{n}{\sqrt{T_e + \tau T_i}} \partial_Z v_{\|i}, \tag{2.27}$$

$$\partial_Z \phi = \mp \frac{T_e}{\sqrt{T_e + \tau T_i}} \partial_Z v_{\|i}, \tag{2.28}$$

$$\partial_Z T_e = \partial_Z T_i = 0, \tag{2.29}$$

$$\omega = -\frac{T_e}{T_e + \tau T_i}[(\partial_Z v_{\|i})^2 \pm \sqrt{T_e + \tau T_i} \, \partial_{ZZ}^2 v_{\|i}], \tag{2.30}$$

where $\Lambda = 3$. The top (bottom) sign refers to the magnetic field pointing towards (away from) the target plate.

The numerical implementation of (2.1)–(2.7) with the boundary conditions given by (2.25)–(2.30) in the GBS code is detailed in Paruta *et al.* (2018). The differential operators in (2.16)–(2.20) are discretized with a fourth-order finite difference scheme on a non-field-aligned grid, which allows for simulations in arbitrary magnetic configurations. The GBS code was verified with the method of manufactured solutions (Riva *et al.* 2014). Convergence studies carried out by Paruta *et al.* (2018) show that the numerical convergence is retrieved with the considered grid resolution.

3. Overview of simulation results

We report a set of GBS simulations carried out with the following parameters: $\rho_*^{-1} = 500$, $a/R_0 \simeq 0.3$, $\tau = 1$, $\eta_{0,e} = 5 \times 10^{-3}$, $\eta_{0,i} = 1$, $L_R = 600$, $L_Z = 800$, $s_{n0} = 0.3$, $\Delta_n = 800$, $\Delta_T = 720$ and $Z_1 = -640 \, \rho_{s0}$. The parallel and perpendicular thermal conductivities are considered constant parameters: $\chi_{\|e} = \chi_{\|i} = 1$ and $\chi_{\perp e} = \chi_{\perp i} = 6$. We vary s_{T0} and ν_0, considering $s_{T0} = \{0.075, 0.15, 0.3, 0.6\}$ and $\nu_0 = \{0.2, 0.6, 0.9, 2.0\}$. We consider the same values s_{T0} for both the ion and electron temperature source, although it should be noted that experimental observations (Ryter *et al.* 2014, 2015) show the importance of the ion heat channel with respect to the electron one in the physics of the L–H transition. The ion-∇B drift direction points upwards (unfavourable for H-mode access) in all the simulations except the ones considered in § 5.1, where the effect of the toroidal magnetic field direction is discussed. The value of the plasma current I_p and the width of its Gaussian distribution σ are chosen to have the safety factors $q_0 \simeq 1$ at the magnetic axis and $q_{95} \simeq 4$ at the tokamak edge. The value of the current in the filament is chosen to be equal to the plasma current. To connect these parameters to a physical case, we can consider typical values at the separatrix of a TCV L-mode discharge (tokamak major radius $R_0 \simeq 0.9$ m and toroidal magnetic field at the tokamak axis $B_T \simeq 1.4$ T) as reference density and electron temperature, i.e. $n_0 \simeq 10^{19}$ m^{-3} and $T_{e0} \simeq 20$ eV, which lead to a size of the simulation domain in physical units of $L_R \simeq 30$ cm, $L_Z \simeq 40$ cm and $R_0 \simeq 25$ cm, which is approximately 1/3 of the TCV size. Regarding the numerical parameters, the grid used is

$N_R \times N_Z \times N_\varphi = 240 \times 320 \times 80$ and the time step is 2×10^{-5}. After an initial transient, the simulations reach a global turbulent quasi-steady state, that results from the interplay among the sources in the closed flux surface region, the turbulence that transports plasma and heat from the core to the SOL, and the losses at the vessel.

An example of typical simulation results is shown in figure 2 (more precisely, we consider the case $s_{T0} = 0.15$ and $\nu_0 = 0.2$). We note that the equilibrium density $\bar{n}$ is a factor of approximately 20 larger in the core than in the near SOL and a factor of 100 larger than in the far SOL (for any quantity f, we define its equilibrium value $\bar{f}$ as its time and toroidal average and the fluctuating component as $\tilde{f} = f - \bar{f}$). The equilibrium electrostatic potential $\bar{\phi}$ is positive in the SOL, while it drops and becomes negative inside the LCFS. The relative fluctuations of the density $\tilde{n}/\bar{n}$, shown by a typical snapshot, reveal that turbulence develops at the tokamak edge and propagates to the near SOL, with a strong interplay between these two regions. In agreement with experimental observations (Terry *et al.* 2003; Garcia *et al.* 2007; Tanaka *et al.* 2009; D'Ippolito, Myra & Zweben 2011), the low-field side (LFS) of the far SOL is characterized by the presence of blobs, coherent radially propagating structures, whose dynamics in GBS simulations is analysed by Nespoli *et al.* (2017), Paruta *et al.* (2019) and Beadle & Ricci (2020). Indeed, as revealed by the study of standard deviation of the density fluctuations, the SOL is characterized by large fluctuations with amplitude comparable to the equilibrium quantities, as in experiments (Horacek, Pitts & Graves 2005; Boedo 2009; Kube *et al.* 2018), while the level of density fluctuations in the core is very low, approximately 1 %, also in agreement with experimental observations (Fontana *et al.* 2017).

By varying the heat source and the collisionality through the parameters s_{T0} and ν_0, respectively, three different turbulent regimes are identified in our simulations: (i) a regime of developed turbulent transport, which we link to the low-confinement mode (L-mode) of tokamak operation, discussed in § 4.1; (ii) a regime of suppressed turbulent transport, with similarities to the high-confinement mode (H-mode), discussed in § 4.2; and (iii) a regime of degraded confinement with catastrophically high turbulent transport, which we associate with the crossing of the density limit and discuss in § 4.3. While the transition from the developed to the suppressed transport regime is rather sharp, the transition to the degraded confinement regime is gradual.

Typical radial profiles at the LFS midplane of the equilibrium pressure, electrostatic potential and $\boldsymbol{E} \times \boldsymbol{B}$ shear are shown in figure 3 for the three regimes. We consider the simulations with $s_{T0} = 0.9$ and $\nu_0 = 0.2$ (suppressed transport regime), $\nu_0 = 0.6$ (developed transport regime), and $\nu_0 = 2.0$ (degraded confinement regime). In the suppressed transport regime, the electrostatic potential drops significantly inside the separatrix, generating a strong $\boldsymbol{E} \times \boldsymbol{B}$ shear across it. This is associated with a steep gradient in the density, electron and ion temperatures. With respect to the suppressed transport regime, in the developed transport regime the electrostatic potential across the separatrix is flatter, the equilibrium $\boldsymbol{E} \times \boldsymbol{B}$ shear is reduced, transport due to turbulence is larger and, consequently, the density and temperature gradient at the tokamak edge is significantly lower. In the degraded confinement regime, turbulent transport is extremely large, leading to a flat profile of density, temperature and electrostatic potential. We note that analogous transitions can be observed by varying the heat source while keeping ν_0 constant.

Typical snapshots of plasma turbulence in the three transport regimes can be seen in figure 4, where the relative density fluctuations and the corresponding normalized standard deviation are shown for the three simulations we are considering. In the case of $\nu_0 = 0.2$, turbulence is localized near the separatrix and, as a consequence of being sheared apart by the strongly varying $\boldsymbol{E} \times \boldsymbol{B}$ radial profile, turbulent structures are elongated along the $\nabla \chi$
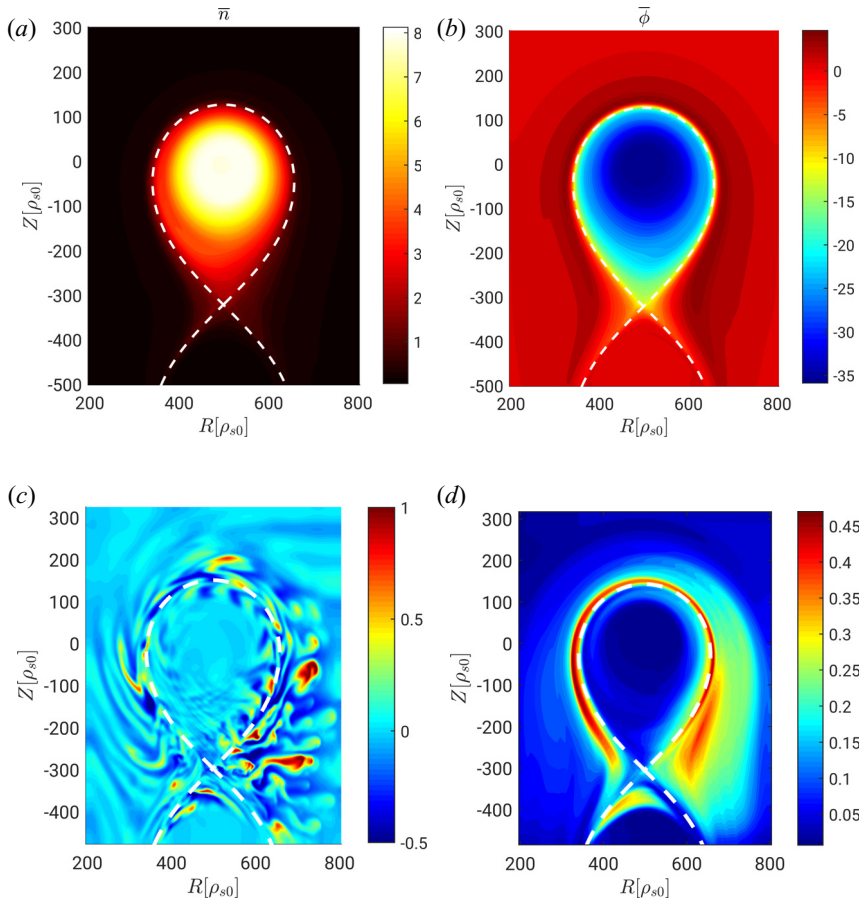
FIGURE 2. Equilibrium density (a), equilibrium electrostatic potential (b), a snapshot of the relative density fluctuations (c) and the normalized standard deviation of the density fluctuations (d) for the simulation with $s_{T0} = 0.15$ and $v_0 = 0.2$. The dashed white line represents the separatrix.
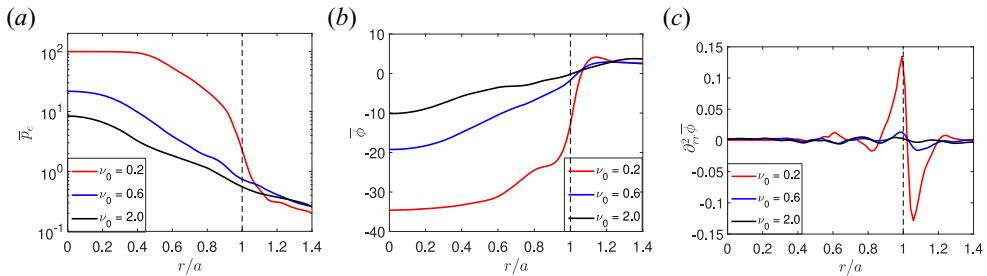

FIGURE 3. Radial profiles at the LFS midplane of the equilibrium pressure (a), equilibrium electrostatic potential (b), and equilibrium $E \times B$ shear (c) for the simulation with $s_{T0} = 0.15$ and $v_0 = 0.2$ (suppressed transport regime), $v_0 = 0.6$ (developed transport regime), and $v_0 = 2.0$ (degraded confinement regime). The radial coordinate is normalized to the radial position a of the separatrix at the midplane.
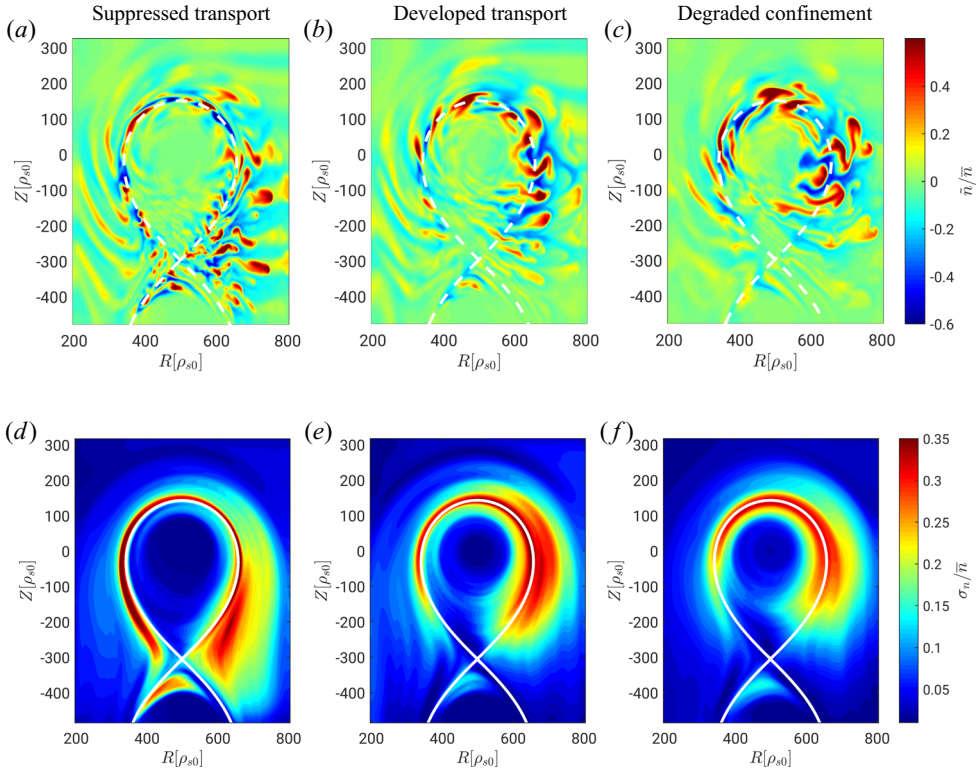
FIGURE 4. Typical snapshots of the relative density fluctuations (*a–c*) and normalized standard deviation of the density fluctuations (*d–f*) for three simulations with $s_{T0} = 0.15$ in the suppressed transport regime, $\nu_0 = 0.2$ (*a,d*), developed transport regime, $\nu_0 = 0.6$ (*b,e*), and degraded confinement regime, $\nu_0 = 2.0$ (*c,f*).

direction, effectively reducing the cross-field transport. The radial extension of turbulent structures is larger for $\nu_0 = 0.6$ and $\nu_0 = 2.0$. In particular, at $\nu_0 = 2.0$, turbulent structures penetrate into the core region. This is in agreement with experimental observations of density fluctuations when the density limit is approached (LaBombard *et al.* 2001). In addition, in the case of $\nu_0 = 0.2$, density fluctuations are generated at both the LFS and high-field side, while, in the other two cases, turbulence mainly develops at the LFS.

In order to highlight the difference in the confinement properties between the different regimes, we compute the electron energy confinement time, $\tau_E = (3(\int_{A_{\mathrm{LCFS}}} \bar{p}_e \, \mathrm{d}R \, \mathrm{d}Z)/2)/\int_{A_{\mathrm{LCFS}}} s_p \, \mathrm{d}R \, \mathrm{d}Z$, for the set of simulations considered in the present study, at different values of S_T and ν_0 (see figure 5). At a given ν_0 or S_T, we note that the simulations in the suppressed transport regime have a higher energy confinement time than the simulations in the developed transport regime. For this reason, we also refer to the developed transport regime as the L-mode and to the suppressed transport regime as the H-mode. The energy confinement time increases by a factor of two from the L-mode to the H-mode, as observed in experiments. In addition, as a consequence of the larger fluctuations, the energy confinement time is lower in the degraded confinement regime than in the developed transport regime.

A detailed analysis of the three regimes is reported in § 4. The power thresholds to access the suppressed transport regime and the degraded confinement regime, both displayed in figure 5 as a function of ν_0, are discussed in § 5.
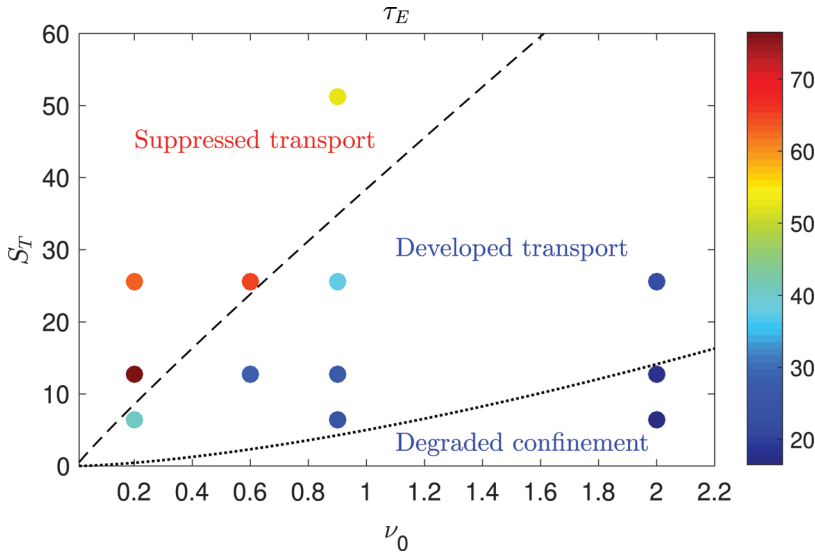
FIGURE 5. Electron energy confinement time for the set of simulations performed for the present study. The dashed black line represents the heat source threshold to access the suppressed transport regime (derived in § 5.1, see (5.7)), while the dotted black line represents the heat source threshold to access the degraded confinement regime (derived in § 5.2, see (5.11)).

4. Turbulent transport regimes at the tokamak edge

In this section, we analyse separately the three transport regimes revealed by our simulations. The mechanisms driving turbulence are studied and an analytical expression of the edge equilibrium pressure gradient length is derived for the different transport regimes.

4.1. *Developed transport regime (L-mode)*

We start by considering the regime of developed transport, which we associate with the L-mode. In this regime, shown by our simulations at intermediate heat source values and intermediate values of collisionality (see figure 5), the shear flow is negligible and turbulent transport results from the nonlinear development of interchange-driven electrostatic ballooning modes (Mosetto *et al.* 2013). This can be verified by removing the interchange drive from the simulations, i.e. by toroidally averaging the term proportional to $C(p_e + \tau p_i)$ in (2.2). The result of this test is displayed in figure 6, where a snapshot of the electron temperature, with and without the interchange drive, is shown for a simulation in the L-mode regime ($s_{T0} = 0.075$ and $\nu_0 = 0.9$). Plasma turbulence is strongly suppressed when the term $C(p_e + \tau p_i)$ is toroidally averaged and, as a consequence, an increase of the equilibrium temperature and pressure gradients is observed. On the other hand, turbulent structures and plasma profiles do not change significantly when the Reynolds stress, i.e. the term $\rho_*^{-1}[\phi, \omega]/B$ appearing in (2.2), is toroidally averaged (see figure 6). This shows that the $E \times B$ shear and the KH instability do not play a major role in the developed transport regime.

In order to provide an analytical estimate of the pressure gradient length in the edge, we follow a procedure similar to the one described by Ricci, Rogers & Brunner (2008), and we balance the perpendicular heat flux crossing the separatrix with the heat source integrated over the volume inside the LCFS. The simulations show that the equilibrium cross-field
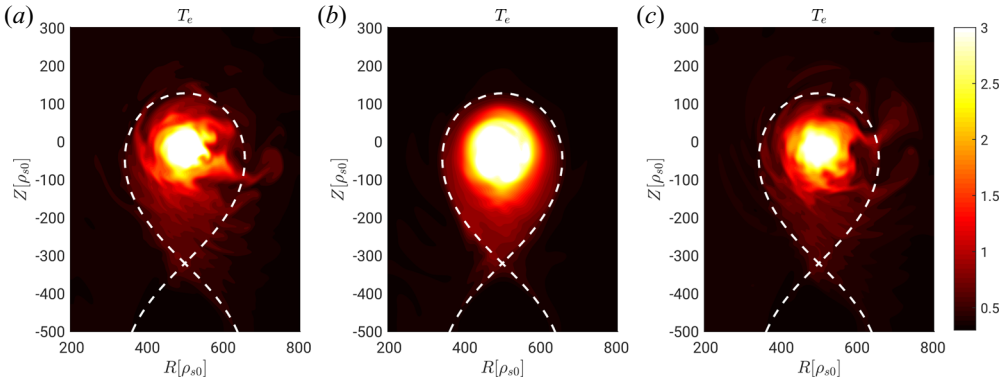
FIGURE 6. A typical snapshot of the electron temperature for the simulation with $s_{T0} = 0.075$ and $\nu_0 = 0.9$ (*a*). Snapshots of simulations with the same parameters but the interchange drive $C(p_e + \tau p_i)$ term in (2.2) toroidally averaged (*b*) and with the KH drive term $\rho_*^{-1}[\phi, \omega]/B$ in (2.2) toroidally averaged (*c*).

heat flux near the separatrix is negligible with respect to the turbulent one, $\bar{p}_e \partial_\chi \bar{\phi} \ll \overline{\tilde{p}_e \partial_\chi \tilde{\phi}}$ (∂_χ denotes the derivative along $\nabla \chi$). Therefore, we focus on the perpendicular turbulent transport, $q_\chi \simeq \overline{\tilde{p}_e \partial_\chi \tilde{\phi}}$, at the LCFS. The quantity $\partial_\chi \tilde{\phi}$ is estimated from the leading terms of the linearized electron pressure equation, which is obtained by linearizing and summing (2.1) and (2.5):

$$\partial_t \tilde{p}_e \sim \rho_*^{-1} \partial_\psi \bar{p}_e \partial_\chi \tilde{\phi} \tag{4.1}$$

(the curvature and parallel gradient terms appearing in (2.1) and (2.5) are significantly smaller than the terms we retain). In (4.1), we estimate the time derivative as the growth rate of the ballooning instability driving the transport, $\gamma_i = \sqrt{2\bar{T}_e/(\rho_* L_p)}$. We also approximate $\partial_\psi \bar{p}_e \simeq \bar{p}_e/L_p$, L_p being the equilibrium pressure gradient length. The resulting expression of $\partial_\chi \tilde{\phi}$ can then be used to evaluate the cross-field interchange-induced heat flux as

$$q_{\psi,i} \sim \rho_* \gamma_i \frac{\tilde{p}_e^2}{\bar{p}_e} L_p. \tag{4.2}$$

The amplitude of the pressure fluctuations appearing in (4.2) can be estimated by observing that the growth of the linearly unstable modes saturates when the instability drive is removed from the system, i.e. $k_\psi \tilde{p}_e \sim \bar{p}_e/L_p$ (Ricci *et al.* 2008; Ricci & Rogers 2013). The perpendicular heat flux is then written as

$$q_{\psi,i} \sim \rho_* \frac{\gamma_i}{k_{\psi,i}^2} \frac{\bar{p}_e}{L_p}. \tag{4.3}$$

Non-local linear calculations show that $k_{\psi,i} \simeq \sqrt{k_{\chi,i}/L_p}$ (Ricci *et al.* 2008). The poloidal wavenumber of the ballooning instability $k_{\chi,i}$ can then be obtained by balancing the interchange driving and the parallel current terms in (2.2). In the parameter regime of our simulations, turbulence is driven by resistive ballooning mode (Mosetto *et al.* 2013). In this case, the resistivity limits the parallel current

(Halpern *et al.* 2013*a*, 2014). This leads to $k_{\chi,i} = (\bar{n}\nu q_{95}^2 \sqrt{\gamma_i})^{-1/2}$. As a consequence, (4.3) becomes

$$q_{\psi,i} \sim \rho_*^{1/4} \sqrt{\bar{n}\nu q_{95}^2} \left(\frac{2\bar{T}_e}{L_p}\right)^{3/4} \bar{p}_e. \tag{4.4}$$

In order to derive the pressure scale length, we note that the heat source integrated over the poloidal plane inside the LCFS corresponds, approximately, to the perpendicular turbulent heat flux crossing the LCFS on a poloidal plane:

$$S_p(R, Z) \simeq \oint_{\text{LCFS}} q_{\psi,i}(R, Z)\,\mathrm{d}l. \tag{4.5}$$

In order to perform the integral on the right-hand side of (4.5), we note that turbulent transport is driven by ballooning modes that develop in the bad-curvature region (see figure 6). As a consequence, we assume that $q_{\psi,i}(R, Z)$ has a constant value at the LCFS on the LFS and vanishes at the high-field side, i.e.

$$S_p \sim \frac{L_\chi}{2} q_{\psi,i}, \tag{4.6}$$

where $L_\chi = \oint_{\text{LCFS}} \mathrm{d}l$ is the length of the LCFS poloidal circumference. The edge equilibrium pressure gradient length is derived using (4.4) and (4.6), that is

$$L_{p,i} \sim \left[\frac{\rho_*}{2}(\nu q_{95}^2 \bar{n})^2 \left(\frac{L_\chi}{S_p}\bar{p}_e\right)^4\right]^{1/3} \bar{T}_e, \tag{4.7}$$

where $\bar{n}$, $\bar{T}_e$ and $\bar{p}_e$ are evaluated at the LCFS.

In figure 7, the ratio of L_p, the equilibrium pressure gradient length directly obtained from the simulations, to $L_{p,i}$, the interchange estimate in (4.7), is displayed for the different values of S_T and ν_0 considered in the present study. At low values of S_T and high values of ν_0, $L_p/L_{p,i} \simeq 1$, revealing a good agreement between the analytical estimate in (4.7) and the simulation result. Hence, in the developed transport regime (as well as in the degraded confinement regime, as discussed in §4.3), turbulence is driven by the interchange instability, the effect of the shear flow not being significant. In addition, since the formation of a pedestal is not observed in this regime, we associate this parameter region with the L-mode. On the other hand, for high values of the heat source and low values of ν_0, the pressure gradient length of the simulations is larger than the value predicted by (4.7), $L_p/L_{p,i} > 1$, meaning that a mechanism different from the interchange instability is responsible for driving turbulent transport and setting the equilibrium pressure gradient length.

It should be noted that, despite being still described as the result of the development of the interchange instability, transport might become catastrophically large at high values of ν_0 and low heat source values, with turbulent eddies that extend from the edge towards the tokamak core, a behaviour that we associate with the crossing of the density limit and we identify as the degraded confinement regime.

4.2. *Suppressed transport regime (H-mode)*

As shown in figure 3, the equilibrium edge electrostatic potential profile in the suppressed transport regime is significantly different from the one in the developed transport regime. This has strong consequences on the nature of turbulent transport. Hence, we focus on the mechanisms that set the $\bar{\phi}$ profile.
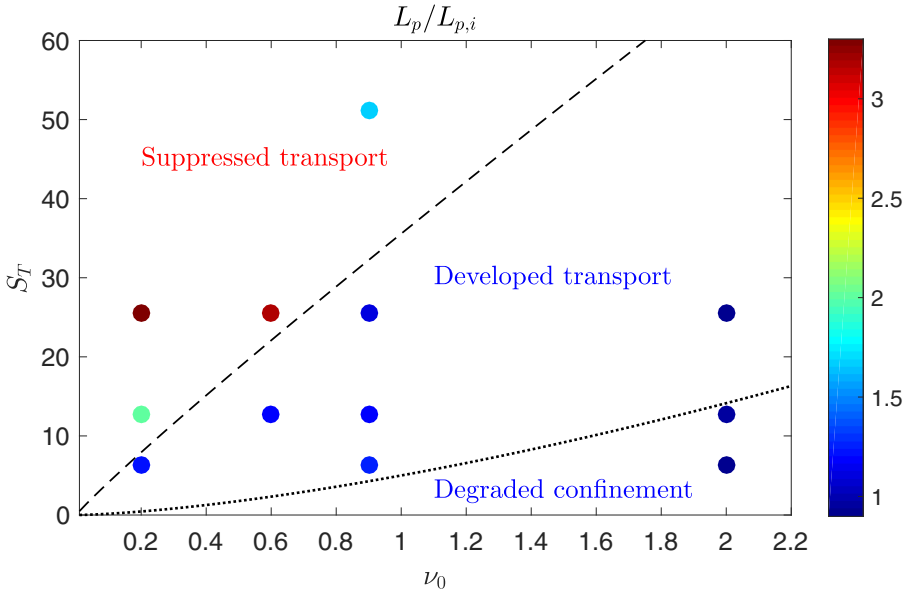
FIGURE 7. Ratio of L_p, the equilibrium pressure gradient length directly obtained from the simulations, to $L_{p,i}$, the estimate in (4.7) based on the assumption that transport is driven by the interchange instability, for all the simulations considered in the present study. The dashed black line represents the heat source threshold to access the suppressed transport regime (see (5.7)), while the dotted black line represents the threshold to access the degraded confinement regime (see (5.11)).

Inside the LCFS, the radial electric field is proportional to the ion pressure gradient, $\partial_r \bar{\phi} \sim -\partial_r \bar{p}_i / \bar{n}$, as experimentally observed (e.g. Schirmer *et al.* 2006; McDermott *et al.* 2009) and theoretically explained (e.g. Zhu, Francisquez & Rogers 2017). On the other hand, ambipolarity of the plasma flow at the sheath imposes that the electrostatic potential is proportional to the electron temperature, $\bar{\phi} \sim \Lambda \bar{T}_e$, in the SOL, as discussed by Stangeby (2000) and Loizu *et al.* (2013). Therefore, $\bar{\phi}$ radially increases as one moves from the magnetic axis towards the LCFS ($-\partial_r \bar{p}_i / \bar{n} > 0$) and then decreases from the LCFS towards the far SOL ($\partial_r \bar{T}_e < 0$). It follows that $\bar{\phi}$ peaks near the separatrix (see figure 3*b*). As s_{T0} increases or ν_0 decreases, both T_e and T_i increase and, as a consequence, also the $E \times B$ shear flow across the LCFS increases (see figure 3*c*). Because of the $E \times B$ shear, the turbulent eddies in the edge resulting from the interchange instability are sheared along the $\nabla \chi$ direction. Furthermore, when the shearing rate, $\rho_*^{-1} \partial_{rr}^2 \bar{\phi}$, is comparable to γ_i, ballooning turbulence is nonlinearly suppressed (Burrell 1997; Terry 2000). At the same time, the $E \times B$ shear provides the drive of the KH instability through the Reynolds stress (Myra *et al.* 2016). Indeed, our simulations show that, for values of the heat source sufficiently high, when $\rho_*^{-1} \partial_{rr}^2 \bar{\phi} > \gamma_i$, the interchange instability is suppressed in the edge and the KH instability becomes the primary instability driving the turbulent transport (Rogers & Dorland 2005; Myra *et al.* 2016).

Figure 8 displays a typical snapshot of the electron temperature for a simulation in the suppressed transport regime ($s_{T0} = 0.6$ and $\nu_0 = 0.9$) and compares it to two simulations having the same parameters, but with the KH and ballooning drives removed. Turbulence is strongly suppressed when the Reynolds stress is toroidally averaged. On the other hand, no significant effect on turbulence is noticed when the interchange drive is removed. This shows that the KH instability is the main drive of turbulent transport and,
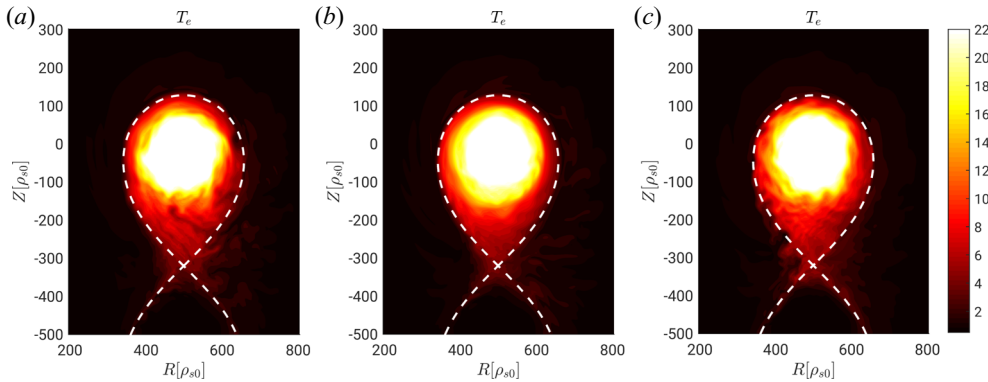
FIGURE 8. A typical snapshot of the electron temperature for the simulation with $s_{T0} = 0.6$ and $\nu_0 = 0.9$ (*a*). Snapshots of simulations with the same parameters but the KH drive term $\rho_*^{-1}[\phi, \omega]/B$ in (2.2) toroidally averaged (*b*) and with the interchange drive term $C(p_e + \tau p_i)$ in (2.2) toroidally averaged (*c*).

consequently, regulates the equilibrium pressure gradient in the suppressed transport regime.

An analytical estimate of the equilibrium pressure gradient length in the edge when turbulence is driven by the KH instability can be derived by following a procedure similar to the one detailed in § 4.1 and discussed for a linear device by Rogers & Ricci (2010). The growth rate of the KH instability is proportional to the $E \times B$ shear (Myra *et al.* 2016), $\gamma_{KH} \sim \rho_*^{-1} \partial_{rr}^2 \bar{\phi} \sim \rho_*^{-1} \bar{T}_e/L_p^2$, having assumed $L_\phi \sim L_p$. The KH mode being a global one, the size of the turbulent eddies it generates is comparable to the pressure gradient length, $k_{\psi, KH} \sim 1/L_p$. Therefore, similarly to (4.3), the KH-driven heat flux can be expressed as

$$q_{\psi, KH} \sim \frac{\bar{T}_e \bar{p}_e}{L_p}. \tag{4.8}$$

By balancing the heat source integrated over the region inside the LCFS and the perpendicular turbulent heat flux crossing the LCFS, similarly to (4.5), but assuming that $q_{\psi, KH}$ is approximately uniform along the LCFS, we obtain

$$L_{p, KH} \sim \frac{\bar{p}_e \bar{T}_e}{4 S_p} L_\chi, \tag{4.9}$$

where $\bar{T}_e$ and $\bar{p}_e$ are evaluated at the LCFS.

The ratio of L_p, the equilibrium pressure gradient length directly obtained from the simulations, to $L_{p, KH}$, the estimate in (4.9), is displayed in figure 9 for the different simulations considered in the present study. At large values of S_T and small values of ν_0, a region can be identified where $L_{p, KH}$ well reproduces the simulation results. In fact, the results of figures 7 and 9 show that turbulent transport is driven by the KH instability in the suppressed transport regime, otherwise the interchange instability regulates the equilibrium pressure gradient length. Furthermore, we note that $L_p > L_{p, KH}$ in the ballooning-driven parameter region, while $L_p > L_{p,i}$ in the suppressed transport regime, as expected from the fact that the mode driving turbulence minimizes the pressure gradient.

The suppressed transport regime shows some of the main key aspects observed experimentally in H-mode discharges, such as the presence of a strong sheared flow
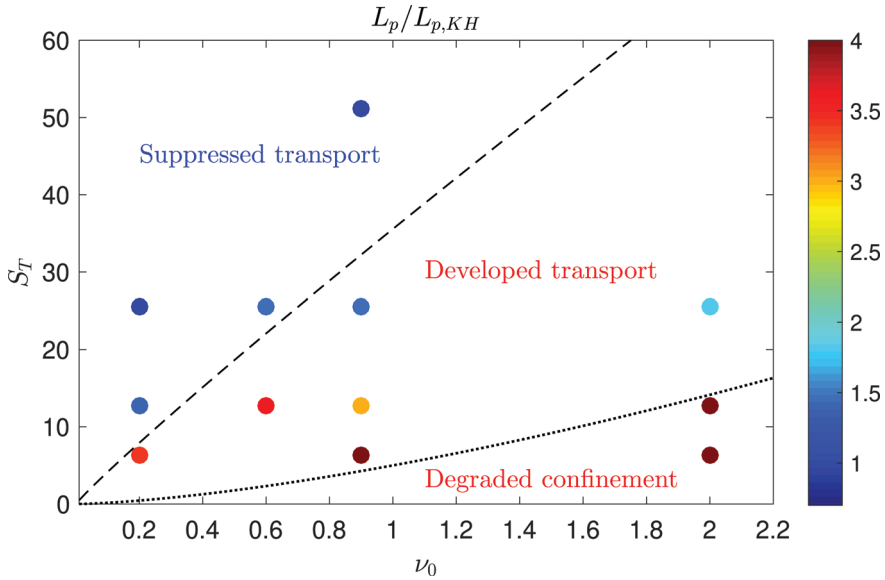
FIGURE 9. Ratio of L_p, the equilibrium pressure gradient length directly obtained from the simulations, to $L_{p,\mathrm{KH}}$, the estimate in (4.9) based on the assumption that the transport is driven by the KH instability, for all the simulations considered in the present study. The dashed black line represents the heat source threshold to access the suppressed transport regime (see (5.7)), while the dotted black line represents the threshold to access the degraded confinement regime (see (5.11)).

(see figure 3c), the reduction of the turbulence level with respect to the L-mode that leads to the formation of a transport barrier near the separatrix (see figure 3a), and the increase of the energy confinement time (see figure 5). All this occurs when a power threshold is exceeded, as detailed in § 5.1. We therefore associate the suppressed transport regime with the H-mode of tokamak operation.

4.3. *Degraded confinement regime*

Figures 4 and 5 show that plasma turbulence and confinement properties strongly vary also within the interchange-driven turbulent regime. In general, for high values of ν_0 and low values of s_{T0}, poor confinement properties and a catastrophically large turbulent transport are observed. Indeed, in this parameter regime, despite being described as the nonlinear development of a ballooning mode, turbulence results in high-level fluctuations, with amplitude comparable to the equilibrium quantity, that propagate from the edge to the core region, as shown in figure 4. This is due to the fact that the radial size of the turbulent structures increases with ν_0, since $k_{\chi,i} \propto \nu_0^{-1/2}$ and $k_{\psi,i} \simeq \sqrt{k_{\chi,i}/L_{p,i}} \propto \nu_0^{-7/12}$. Figure 10 shows the radial extension of turbulent eddies normalized to the tokamak minor radius for the different simulations considered in the present study. In particular, if the value of ν_0 is sufficiently large and s_{T0} sufficiently small, turbulent eddies appear to have a size comparable to the tokamak minor radius, i.e. $k_\psi a \sim 1$. As a consequence, they extend towards the core region and lead to a very large cross-field turbulent transport throughout the closed field line region. In these conditions, the core temperature can significantly drop and magnetohydrodynamic modes, which are beyond the description provided by our model, can play an important role (Greenwald *et al.* 1988; Greenwald 2002). As already mentioned in § 3, the degraded confinement regime is linked to high values of the density
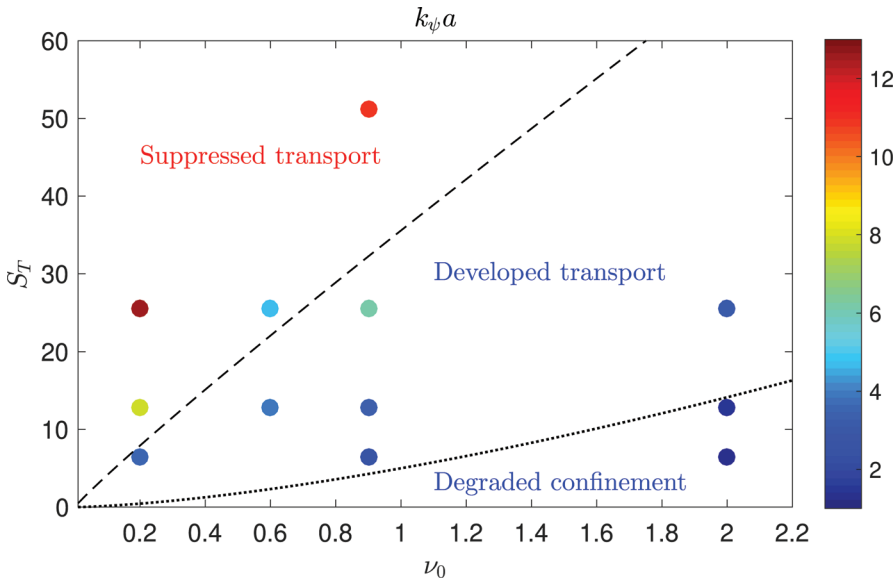
FIGURE 10. Radial wavenumber computed from the correlation length of turbulent eddies, normalized to the tokamak minor radius, for all the simulations considered in the present study. The dashed black line represents the heat source threshold to access the suppressed transport regime (see (5.7)), while the dotted black line represents the threshold to access the degraded confinement regime (see (5.11)).

and we associate it with the crossing of the density limit, in agreement with the result of Hajjar *et al.* (2018). Experimental evidences that the density limit is due to an increase of edge collisionality, proportional to ν_0 in the model considered, are reported from the TJ-K stellarator (Schmid *et al.* 2017).

Three main effects are observed when crossing the density limit. First, the $E \times B$ shear near the separatrix in the degraded confinement regime is even weaker than in the developed transport regime, as shown in figure 3(*c*). This is in agreement with recent experiments that show how the edge shear flow collapses when the density limit is approached (Hong *et al.* 2017). Therefore, the $E \times B$ shear is an important quantity not only to explain the transition from the developed transport regime to the suppressed transport regime, but also to recognize the crossing of the density limit. Second, the degraded confinement regime is characterized by a flatter equilibrium density profile in the SOL with respect to the developed and suppressed transport regimes (see figure 11). In fact, the blob size increases with the collisionality (D'Ippolito *et al.* 2011; Nespoli *et al.* 2017; Beadle & Ricci 2020), leading to an enhancement of the cross-field turbulent transport in the far SOL. The density profile becomes flatter with no clear distinction between the edge, near SOL and far SOL. Experimental observations of the flattening of the density profiles as the density increases towards the density limit are reported by LaBombard *et al.* (2001). Third, the large-amplitude fluctuations that extend towards the core region lead to a strong enhancement of cross-field turbulent transport and the loss of confinement.

5. Transition threshold between transport regimes

In this section, we focus on the transition from the developed transport regime to the suppressed transport regime, which we associate with the L–H transition, and from the
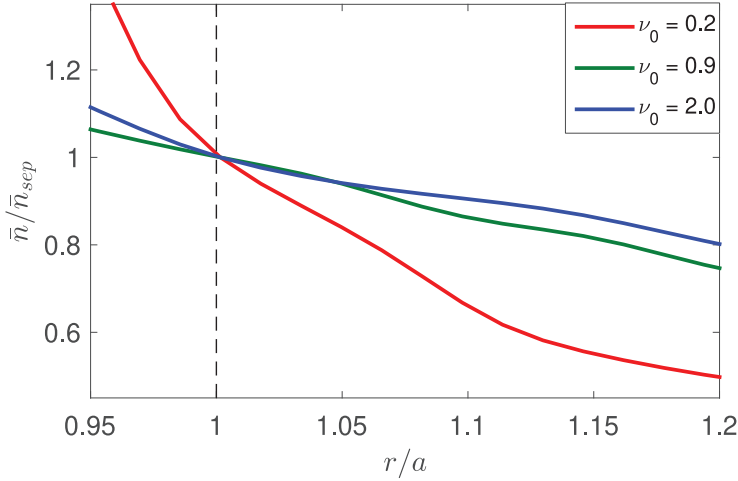
FIGURE 11. Equilibrium density radial profile at the outboard midplane for simulations at $s_{T0} = 0.075$ and various values of ν_0.

developed transport regime to the degraded confinement regime, which we associate with the crossing of the density limit. Analytical estimates of the heat source threshold to access the suppressed transport regime and of the density threshold to access the degraded confinement regime are derived.

5.1. *Heat source threshold to access the suppressed transport regime*

The transition from the L-mode to the H-mode occurs when $L_{p,i} \simeq L_{p,\text{KH}}$, namely when the turbulent transport due to the interchange instability equals the one due to the KH instability. An estimate of S_p at the transition can be derived by equating (4.7) and (4.9):

$$S_p^{\text{LH}} \sim \rho_* L_\chi \nu_0^2 q_{95}^4 \bar{n}^3 / (2\bar{T}_e), \tag{5.1}$$

where $\bar{n}$ and $\bar{T}_e$ are evaluated at the LCFS. The relation between $\bar{T}_e$ at the LCFS and S_p can be obtained by balancing S_p with the parallel losses to the vessel walls. As an order of magnitude estimate, this balance can be expressed by using the integral of the heat flux over the SOL width, Δ_{SOL}, as

$$\int_{\Delta_{\text{SOL}}} \bar{p}_e \bar{c}_s \, \mathrm{d}l \sim S_p, \tag{5.2}$$

having assumed to be in the sheath connected regime (i.e. no temperature drop in the divertor region) and assuming that the plasma outflows at the divertor plate with the sound speed. Furthermore, by assuming that the pressure and temperature decay exponentially in the SOL on L_p scale, (5.2) becomes

$$\bar{T}_e \sim \left(\frac{2S_p}{\bar{n}L_p} \right)^{2/3}, \tag{5.3}$$

with $\bar{T}_e$ and $\bar{n}$ evaluated at the LCFS. Equations (5.1) and (5.3) allow us to derive an analytical estimate of the heat source threshold for H-mode access,

$$S_p^{\text{LH}} \sim \rho_*^{7/15} (\nu_0 q_{95}^2)^{14/15} L_\chi^{11/15} \bar{n}^{29/15}, \tag{5.4}$$

the corresponding electron temperature at the LCFS,

$$T_e^{\text{LH}} \sim \rho_*^{4/15}(\nu_0 q_{95}^2)^{8/15}L_\chi^{2/15}\bar{n}^{8/15}, \tag{5.5}$$

and the equilibrium pressure gradient length at the transition,

$$L_p^{\text{LH}} \sim \rho_*^{1/15}(\nu_0 q_{95}^2)^{2/15}L_\chi^{8/15}\bar{n}^{2/15}. \tag{5.6}$$

In (5.4), the increase of the heat source required to access the H-mode with ν_0 is due to the increase of cross-field turbulent transport in the developed transport regime. Indeed, $q_{\psi,i}$ is proportional to $\nu_0^{1/2}$ (see (4.4)) and $L_{p,i}$ is proportional to $\nu_0^{2/3}$ (see (4.7)).

We now compare our analytical estimate with the simulation results. For this purpose, we express (5.4) in terms of S_T, by using $S_T^{\text{LH}} \simeq S_p^{\text{LH}}/\bar{n}$, and we obtain

$$S_T^{\text{LH}} \sim \rho_*^{7/15}(\nu_0 q_{95}^2)^{14/15}L_\chi^{11/15}\bar{n}^{14/15}. \tag{5.7}$$

The analytical estimate of the threshold S_T^{LH} as a function of ν_0 (assuming a constant value for the normalized density $\bar{n}$ at the LCFS) is displayed in figure 9, showing a very good agreement between the analytical prediction of (5.7) and the simulation results.

We also link our L–H transition with experimental observations. In order to identify the scaling of S_p^{LH} with the main experimental parameters, we write the power threshold in (5.4) in physical units as

$$P_{\text{LH}} = 2\pi R_0 S_p^{\text{LH}} \simeq 9 \times 10^7 \left(\frac{m_e}{m_i}\right)^{9/15} n^{29/15}R_0^{22/15}q_{95}^{28/15}a^{11/15}B_T^{-11/15}$$

$$\simeq 9 \times 10^7 \left(\frac{m_e}{m_i}\right)^{0.6} n^{1.9}R_0^{1.5}q_{95}^{1.9}a^{0.7}B_T^{-0.7}, \tag{5.8}$$

with the $2\pi R_0$ factor taking into account the integration of the heat source along the toroidal direction, having imposed $L_\chi \sim 2\pi a$, and the density at the LCFS being expressed in units of 10^{20} m^{-3}. The scaling law in (5.8) correctly reproduces the isotope effect observed in experiments (Righi *et al.* 1999; Maggi *et al.* 2017) and also found in previous theoretical investigations (De Dominici *et al.* 2019). The dependence on a and R_0 shows a good agreement with the experimental scaling law in (1.1). The exponent of the density in (5.8) is a factor of approximately 2.7 larger than the one predicted by the experimental scaling law in (1.1), although we remark that the density in (5.8) is evaluated at the LCFS, while the density in (1.1) denotes the line-averaged density. The power threshold in (5.8) depends inversely on the toroidal magnetic field, while the experimental scaling law in (1.1) shows a direct dependence on B_T. Moreover, in contrast to the experimental scaling law in (1.1), the power threshold in (5.8) depends on q_{95}.

As an example of the evaluation of (5.8) in experimental conditions, we consider the value of the power threshold predicted for typical parameters of the TCV tokamak ($a = 0.25$ m, $R_0 = 0.88$ m, line-averaged density $n_e \simeq 4 \times 10^{19}$ m^{-3}, density at the LCFS $n \simeq 2 \times 10^{19}$ m^{-3}, $B_T \simeq 1.4$ T, and $q_{95} \simeq 4$). The estimate in (5.8) gives $P_{\text{LH}} \simeq 142$ kW, a power threshold that has the same order of magnitude as the experimental TCV power threshold, $P_{\text{LH}} \simeq 260$ kW (e.g. Scaggion *et al.* 2012; Martin *et al.* 2014).

Experimental measurements show that the power to access the H-mode is lower when the ion-∇B drift direction is towards the X-point, rather than away from it (ASDEX
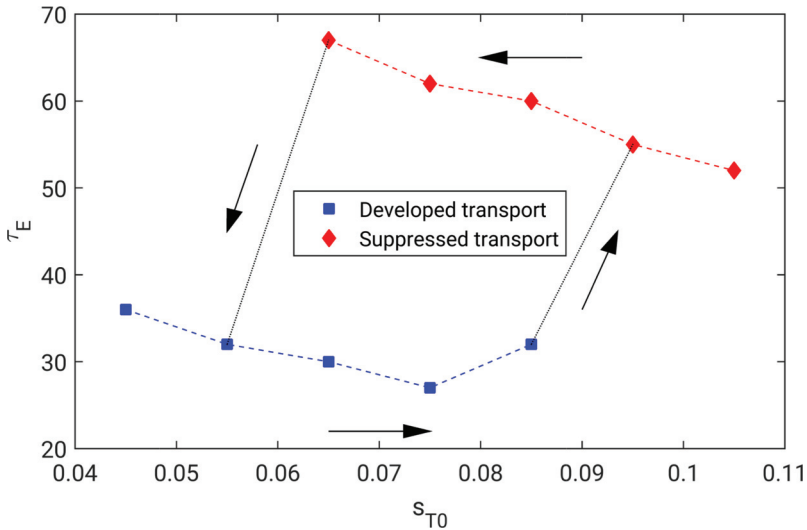
FIGURE 12. Energy confinement time for simulations with $\nu_0 = 0.2$ and various values of s_{T0}. Simulations in the developed transport regime are denoted by blue squares and in the suppressed transport regime by red diamonds. Starting from a simulation in the developed transport regime, s_{T0} is progressively increased from 0.045 to 0.105. The transition to the suppressed transport regime occurs approximately at $s_{T0} \simeq 0.085$. The heat source is then progressively reduced until the reverse transition occurs, approximately at $s_{T0} \simeq 0.065$. The transitions are represented as dotted black lines.

Team 1989). In order to study the dependence of the heat source threshold on the ion-∇B drift direction, we consider two simulations where we vary the direction of the toroidal magnetic field while keeping the same direction of the plasma current and other parameters the same. In particular, we consider $s_{T0} = 0.3$ and $\nu_0 = 0.9$, parameters close to the L–H transition when the ion-∇B drift direction points upwards (unfavourable for H-mode access). The equilibrium density, temperature and $\boldsymbol{E} \times \boldsymbol{B}$ shear profiles at the LFS midplane do not show significant differences between the simulations with favourable and unfavourable ion-∇B drift direction, both simulations belonging to the developed transport regime. Therefore, at least in the case analysed, the power threshold to access the H-mode is independent of the toroidal magnetic field direction in our model. The discrepancy between experimental and simulation observations may be due to the absence of kinetic effects involving passing and trapped particles; among these we mention the effects of ion orbit loss, which can be important in establishing the dependence of the L–H transition on the ion-∇B drift direction (Stoltzfus-Dueck 2012; Boedo *et al.* 2016), as also pointed out by XGC1 simulations (Ku *et al.* 2018).

Experimental observations (Snipes *et al.* 1996; Thomas *et al.* 1998) and theoretical models (Hinton 1991; Drake *et al.* 1996) point out the presence of hysteresis on the power threshold for the L–H transition, i.e. having entered the H-mode conditions, the hysteresis allows for a decrease of the power below the threshold for H-mode access without inducing the H–L transition. The presence of hysteresis in our simulations is investigated by performing a set of simulations at $\nu_0 = 0.2$ and various values of s_{T0} in the proximity of the threshold to access the suppressed transport regime (more precisely we consider $s_{T0} = 0.045, 0.055, 0.065, 0.075, 0.085, 0.095, 0.105$). Starting from a simulation in the developed transport regime, s_{T0} is progressively increased from 0.045 to 0.105 where the transition to the suppressed transport regime occurs. Then, using the simulation at

$s_{T0} = 0.105$ in the suppressed transport regime as initial condition, we perform a second set of simulations where s_{T0} is progressively reduced, observing the H–L transition at $s_{T0} \simeq 0.065$ (see figure 12). Therefore, the transition from the developed transport regime to the suppressed transport regime occurs at a higher value of the heat source than the reverse transition, thus pointing out the presence of hysteresis in the considered model.

The presence of hysteresis can be explained as follows. In the suppressed transport regime, the $E \times B$ shear is strong near the separatrix and the turbulent transport is mainly driven by the KH instability. As the heat source decreases, the equilibrium pressure gradient decreases (see (4.9)) as well as the $E \times B$ shear near the separatrix. However, the $E \times B$ shear remains sufficiently strong to stabilize ballooning modes, thus allowing for a decrease of the heat source below the L–H transition threshold with no collapse of the $E \times B$ shear. This collapse is suddenly followed by the onset of the interchange instability, with the developed transport regime eventually reached.

As an aside observation of figure 12, we note that, within the same transport regime, the energy confinement time decreases as the heat source increases, the only exception being the simulation at $s_{T0} = 0.085$ in the developed transport regime, which is in the proximity of the transition. The decrease of the energy confinement time following the increase of the heat source is also observed in many experiments (Yushmanov *et al.* 1990; Cordey *et al.* 2005).

5.2. *Density threshold to access the degraded confinement regime*

In our simulations, the transition to the degraded confinement regime occurs gradually as the edge fluctuations present in the developed transport regime reach a size comparable to the system size, $1/k_\psi \sim a$, and the equilibrium pressure gradient length becomes comparable to the tokamak minor radius, $L_p \sim a$. This last observation can be considered as a condition to access the regime of degraded confinement. By assuming interchange-driven turbulent transport, this condition can be expressed as

$$a \sim L_{p,i} \sim \left[\frac{\rho_*}{2} (\nu q_{95}^2 \bar{n})^2 \left(\frac{2\pi a}{S_p} \bar{p}_e \right)^4 \right]^{1/3} \bar{T}_e, \tag{5.9}$$

having estimated the equilibrium pressure gradient length according to (4.7), and $\bar{n}$ and $\bar{T}_e$ being evaluated at the LCFS. By using the estimate of the electron temperature in (5.3), we obtain

$$S_p \sim \rho_*^{3/4} \frac{8\pi^3}{a^{5/4}} (\nu_0 q_{95}^2)^{3/2} \bar{n}^{5/2}. \tag{5.10}$$

In order to compare (5.10) with the simulation results, we express (5.10) in terms of S_T, again using $S_p \simeq S_T/\bar{n}$, and we find

$$S_T \sim \rho_*^{3/4} \frac{8\pi^3}{a^{5/4}} (\nu_0 q_{95}^2)^{3/2} \bar{n}^{3/2}. \tag{5.11}$$

The analytical prediction of temperature source threshold in (5.11) is plotted in the phase space of figure 10, by keeping constant the normalized density at the LCFS (this value is approximately constant in the simulations considered in the present study). A good agreement between the simulation results and the theoretical estimate is shown by the analysis of the radial extension of the turbulent eddies.

For comparison with experimental results, the heat source threshold in (5.10) can be written in physical units as

$$S_p \simeq 3.2 \left(\frac{m_i}{m_e}\right)^{1/4} \frac{a^{19/4} n^{5/2}}{I_p^3 R_0^{9/4}}, \tag{5.12}$$

where S_p is expressed in kW m^{-1} and n in 10^{20} m^{-3}, I_p is the plasma current (in MA) and we have used $q_{95} \sim 2\pi a^2 B_T/(R_0 I_p)$. The density threshold to access the degraded confinement regime, corresponding to the operational density limit evaluated at the LCFS, can then be derived from (5.12) and, in physical units, takes the following form:

$$n \simeq 0.3 \left(\frac{m_e}{m_i}\right)^{1/10} P_{\text{sep}}^{2/5} R_0^{1/2} \frac{I_p^{6/5}}{a^{19/10}} \simeq 0.3 \left(\frac{m_e}{m_i}\right)^{0.1} P_{\text{sep}}^{0.4} R_0^{0.5} \frac{I_p^{1.2}}{a^{1.9}}, \tag{5.13}$$

where $P_{\text{sep}} = 2\pi R_0 S_p$ is the power crossing the separatrix (in kW), with I_p in MA and n in 10^{20} m^{-3}. The comparison between the analytical scaling law of (5.13) and the empirical scaling in (1.2) is not straightforward since we have expressed the density limit in terms of the density at the LCFS, while the empirical scaling refers to the line-averaged density. With this caveat in mind, we note that (5.13) reproduces the dependence on the plasma current and tokamak minor radius expected by the experimental scaling law of (1.2). The dependence on the ion mass is weak, in agreement with experimental observations that do not show evident isotope effect on the density limit (Saibene *et al.* 1999). The analytical scaling law of (5.13) depends on the heat source, a feature also observed in some experiments (Stabler *et al.* 1992; Mertens *et al.* 1997). For instance, it has been experimentally found (Mertens *et al.* 1997) that, at the density limit, the density at the LCFS depends on the power crossing the separatrix as $n \propto P_{\text{sep}}^{0.6}$, in good agreement with the power dependence in (5.13). However, the analytical density threshold of (5.13) depends also on the tokamak major radius, while the empirical scaling in (1.2) is independent of it. As an example of application of (5.13), we note that the threshold density predicted for the TCV tokamak ($a = 0.25$ m, $R_0 = 0.88$ m, $I_p = 1$ MA and $P_{\text{sep}} = 100$ kW) is $n \simeq 10^{21}$ m^{-3}.

6. Conclusions

In the present paper, results of flux-driven simulations in realistic single-null geometry, carried out using the GBS code with the domain encompassing the whole tokamak to retain the core–edge–SOL interplay, are used to study the important role of sources and resistivity in driving a variety of turbulent transport regimes in the tokamak edge. Our simulations show the presence of three turbulent transport regimes: a regime of developed turbulent transport, which we link to the L-mode observed in the experiments; a regime of suppressed turbulent transport, with similarities to the H-mode; and a regime of degraded confinement, which we associate with the crossing of the density limit. The developed transport and degraded confinement regimes appear at low heat source and high resistivity, with turbulent transport driven by the interchange instability, while the suppressed transport regime appears at high heat source and low resistivity, with turbulent transport driven by the KH instability. The energy confinement time in the suppressed transport regime is a factor of approximately two higher than in the developed transport regime. An overall loss of confinement is observed in the degraded confinement regime, with strong fluctuations that reach the tokamak core. An analytical expression of the equilibrium pressure gradient length in the tokamak edge is derived for all the transport regimes.

The transition from the developed to the suppressed transport regime shows many features in common with the L–H transition observed experimentally, such as the presence of a strong sheared flow, the reduction of the turbulence level, the formation of a transport barrier near the separatrix and the presence of a power threshold. The power threshold for H-mode access derived herein is able to reproduce the isotope effect and the experimental parameter scaling of (1.1), with the exception of the toroidal magnetic field and the dependence on safety factor. In addition, no dependence of the power threshold on the ion-∇B direction is observed in the considered simulations. The transition from the developed to the suppressed transport regime is subject to hysteresis as it occurs at a higher value of the heat source with respect to the inverse transition. The analytical prediction of the power threshold shows a good agreement with the results of GBS simulations performed with various values of heat source and resistivity (see figure 5).

In the degraded confinement regime, found at high values of resistivity and low heat source, turbulent transport is driven by the interchange instability with turbulent eddies of size comparable to the tokamak minor radius. High-level fluctuations are generated in the core and the particle confinement time drops. We derive an analytical estimate of the density threshold to access the degraded confinement regime, which we associate with the operational Greenwald density limit. Indeed, it retrieves the main dependencies on the plasma current and tokamak minor radius observed experimentally (Greenwald 2002).

Finally, we remark that the model considered in this work neglects coupling with neutrals dynamics, neoclassical and kinetic effects. Moreover, it is electrostatic and makes use of the Boussinesq approximation. These terms can definitely have an impact on the edge turbulent regimes. In fact, neutral dynamics may affect the L–H transition dynamics, as shown by Shaing & Hsu (1995), Carreras *et al.* (1996) and Owen *et al.* (1998). In Chôné *et al.* (2014, 2015) and Viezzer *et al.* (2013), it is shown that neoclassical terms play an important role in the radial electric field responsible for the onset of a transport barrier that leads to the L–H transition. Kinetic effects can also be important (Stoltzfus-Dueck 2012; Boedo *et al.* 2016). Electromagnetic effects can play a role in setting the pedestal height and width (Snyder *et al.* 2004, 2009), and the density limit (Rogers *et al.* 1998). In Bodi *et al.* (2011) and Stegmeir *et al.* (2019), the validity of the Boussinesq approximation is addressed and, while the results show that a good agreement exists between the results of turbulence simulations that make use of or avoid the application of the Boussinesq approximation, this result cannot be taken for granted in general. As a future work, we plan to include these effects for a more accurate investigation of the edge turbulent regimes and to study separately the role of the ion and electron temperature source in the transitions.

Acknowledgements

Editor Hartmut Zohm thanks the referees for their advice in evaluating this article.

Declaration of interests

The authors report no conflict of interest.

REFERENCES

ASDEX TEAM. 1989 The H-mode of ASDEX. *Nucl. Fusion* **29** (11), 1959–2040.

BEADLE, C. F. & RICCI, P. 2020 Understanding the turbulent mechanisms setting the density decay length in the tokamak scrape-off layer. *J. Plasma Phys.* **86** (1), 175860101.

BEURSKENS, M. N. A., OSBORNE, T. H., SCHNEIDER, P. A., WOLFRUM, E., FRASSINETTI, L., GROEBNER, R., LOMAS, P., NUNES, I., SAARELMA, S., SCANNELL, R., *et al.* 2011 H-mode pedestal scaling in DIII-D, ASDEX Upgrade, and JET. *Phys. Plasmas* **18** (5), 056120.

BODI, K., CIRAOLO, G., GHENDRIH, P., SCHWANDER, F., SERRE, E. & TAMAIN, P. 2011 Impact of the Boussinesq approximation in tokamak scrape–off layer turbulence. In *38th EPS Conference on Plasma Physics P1.121*.

BOEDO, J. A. 2009 Edge turbulence and SOL transport in tokamaks. *J. Nucl. Mater.* **390**, 29–37.

BOEDO, J. A., DEGRASSIE, J. S., GRIERSON, B., STOLTZFUS-DUECK, T., BATTAGLIA, D. J., RUDAKOV, D. L., BELLI, E. A., GROEBNER, R. J., HOLLMANN, E., LASNIER, C., *et al.* 2016 Experimental evidence of edge intrinsic momentum source driven by kinetic ion loss and edge radial electric fields in tokamaks. *Phys. Plasmas* **23** (9), 092506.

BURRELL, K. H. 1997 Effects of E × B velocity shear and magnetic shear on turbulence and transport in magnetic confinement devices. *Phys. Plasmas* **4** (5), 1499–1518.

CARRERAS, B. A., DIAMOND, P. H. & VETOULIS, G. 1996 Role of neutrals in the phase transition model. *Phys. Plasmas* **3** (11), 4106–4114.

CHANG, C. S., KU, S., TYNAN, G. R., HAGER, R., CHURCHILL, R. M., CZIEGLER, I., GREENWALD, M., HUBBARD, A. E. & HUGHES, J. W. 2017 Fast low-to-high confinement mode bifurcation dynamics in a tokamak edge plasma gyrokinetic simulation. *Phys. Rev. Lett.* **118** (17), 175001.

CHÔNÉ, L., BEYER, P., SARAZIN, Y., FUHR, G., BOURDELLE, C. & BENKADDA, S. 2014 LH transition dynamics in fluid turbulence simulations with neoclassical force balance. *Phys. Plasmas* **21** (7), 070702.

CHÔNÉ, L., BEYER, P., SARAZIN, Y., FUHR, G., BOURDELLE, C. & BENKADDA, S. 2015 Mechanisms and dynamics of the external transport barrier formation in non-linear plasma edge simulations. *Nucl. Fusion* **55** (7), 073010.

CHÔNÉ, L., KIVINIEMI, T. P., LEERINK, S., NISKALA, P. & ROCHFORD, R. 2018 Improved boundary condition for full-f gyrokinetic simulations of circular-limited tokamak plasmas in ELMFIRE. *Contrib. Plasma Phys.* **58** (6–8), 534–539.

CONNOR, J. W. & WILSON, H. R. 2000 A review of theories of the LH transition. *Plasma Phys. Control. Fusion* **42** (1), R1.

CORDEY, J. G., THOMSEN, K., CHUDNOVSKIY, A., KARDAUN, O. J. W. F., TAKIZUKA, T., SNIPES, J. A., GREENWALD, M., SUGIYAMA, L., RYTER, F., KUS, A., *et al.* 2005 Scaling of the energy confinement time with β and collisionality approaching ITER conditions. *Nucl. Fusion* **45** (9), 1078.

DANNERT, T. & JENKO, F. 2005 Gyrokinetic simulation of collisionless trapped-electron mode turbulence. *Phys. Plasmas* **12** (7), 072309.

DE DOMINICI, G., FUHR, G., BEYER, P., BOURDELLE, C., CHÔNÉ, L., CIANFRANI, F., FALCHETTO, G. L., GARBET, X. & SARAZIN, Y. 2019 Flux driven pedestal formation in tokamaks: turbulence simulations validated against the isotope effect. arXiv:1912.09792.

DICKINSON, D., ROACH, C. M., SAARELMA, S., SCANNELL, R., KIRK, A. & WILSON, H. R. 2012 Kinetic instabilities that limit β in the edge of a tokamak plasma: a picture of an H-mode pedestal. *Phys. Rev. Lett.* **108** (13), 135002.

DIF-PRADALIER, G., CASCHERA, E., GHENDRIH, P., DONNEL, P., GARBET, X., GRANDGIRARD, V., LATU, G., NORSCINI, C. & SARAZIN, Y. 2017 Evidence for global edge – core interplay in fusion plasmas. *Plasma Fusion Res.* **12**, 1203012.

DOERK, H., DUNNE, M., JENKO, F., RYTER, F., SCHNEIDER, P. A. WOLFRUM, E. & ASDEX UPGRADE TEAM 2015 Electromagnetic effects on turbulent transport in high-performance ASDEX Upgrade discharges. *Phys. Plasmas* **22** (4), 042503.

DORF, M. & DORR, M. 2020 Progress with the 5D full-F continuum gyrokinetic code COGENT. *Contrib. Plasma Phys.*, e201900113.

DRAKE, J. F., LAU, Y. T., GUZDAR, P. N., HASSAM, A. B., NOVAKOVSKI, S. V., ROGERS, B. & ZEILER, A. 1996 Local negative shear and the formation of transport barriers. *Phys. Rev. Lett.* **77** (3), 494.

DUDSON, B. D., ALLEN, A., BREYIANNIS, G., BRUGGER, E., BUCHANAN, J., EASY, L., FARLEY, S., JOSEPH, I., KIM, M., MCGANN, A. D., *et al.* 2015 BOUT++: recent and current developments. *J. Plasma Phys.* **81** (1), 365810104.

D'IPPOLITO, D. A., MYRA, J. R. & ZWEBEN, S. J. 2011 Convective transport by intermittent blob-filaments: comparison of theory and experiment. *Phys. Plasmas* **18** (6), 060501.

FICHTMÜLLER, M., CORRIGAN, G., SIMONINI, R. & JET JOINT UNDERTAKING 1998 Core-Edge coupling and the effect of the edge on overall plasma performance. *Czechoslov. J. Phys.* **48**, 25–38.

FIELDING, S. J., HUGILL, J., MCCRACKEN, G. M., PAUL, J. W. M., PRENTICE, R. & STOTT, P. E. 1977 High-density discharges with gettered torus walls in DITE. *Nucl. Fusion* **17** (6), 1382.

FONTANA, M., PORTE, L., CODA, S., SAUTER, O. & THE TCV TEAM. 2017 The effect of triangularity on fluctuations in a tokamak plasma. *Nucl. Fusion* **58** (2), 024002.

FREI, B. J., JORGE, R. & RICCI, P. 2020 A gyrokinetic model for the plasma periphery of tokamak devices. *J. Plasma Phys.* **86** (2), 905860205.

GARCIA, O. E., HORACEK, J., PITTS, R. A., NIELSEN, A. H., FUNDAMENSKI, W., NAULIN, V. & RASMUSSEN, J. J. 2007 Fluctuations and transport in the TCV scrape-off layer. *Nucl. Fusion* **47** (7), 667.

GIACOMIN, M., STENGER, L. N. & RICCI, P. 2020 Turbulence and flows in the plasma boundary of snowflake magnetic configurations. *Nucl. Fusion* **60** (2), 024001.

GREENWALD, M. 2002 Density limits in toroidal plasmas. *Plasma Phys. Control. Fusion* **44** (8), R27.

GREENWALD, M., TERRY, J. L., WOLFE, S. M., EJIMA, S., BELL, M. G., KAYE, S. M. & NEILSON, G. H. 1988 A new look at density limits in tokamaks. *Nucl. Fusion* **28** (12), 2199.

GRENFELL, G., VAN MILLIGEN, B. P., LOSADA, U., ESTRADA, T., LIU, B., SILVA, C., SPOLAORE, M., HIDALGO, C., *et al.* 2019 The impact of edge radial electric fields on edge–scrape-off layer coupling in the TJ-II stellarator. *Nucl. Fusion* **60** (1), 014001.

GROEBNER, R. J., BURRELL, K. H. & SERAYDARIAN, R. P. 1990 Role of edge electric field and poloidal rotation in the L–H transition. *Phys. Rev. Lett.* **64** (25), 3015.

HAHM, T. S., WANG, L. & MADSEN, J. 2009 Fully electromagnetic nonlinear gyrokinetic equations for tokamak edge turbulence. *Phys. Plasmas* **16** (2), 022305.

HAJJAR, R. J., DIAMOND, P. H. & MALKOV, M. A. 2018 Dynamics of zonal shear collapse with hydrodynamic electrons. *Phys. Plasmas* **25** (6), 062306.

HALPERN, F. D., JOLLIET, S., LOIZU, J., MOSETTO, A. & RICCI, P. 2013*b* Ideal ballooning modes in the tokamak scrape-off layer. *Phys. Plasmas* **20** (5), 052306.

HALPERN, F. D., RICCI, P., JOLLIET, S., LOIZU, J., MORALES, J., MOSETTO, A., MUSIL, F., RIVA, F., TRAN, T.-M. & WERSAL, C. 2016 The GBS code for tokamak scrape-off layer simulations. *J. Comput. Phys.* **315**, 388–408.

HALPERN, F. D., RICCI, P., JOLLIET, S., LOIZU, J. & MOSETTO, A. 2014 Theory of the scrape-off layer width in inner-wall limited tokamak plasmas. *Nucl. Fusion* **54** (4), 043003.

HALPERN, F. D., RICCI, P., LABIT, B., FURNO, I., JOLLIET, S., LOIZU, J., MOSETTO, A., ARNOUX, G., GUNN, J. P., HORACEK, J., *et al.* 2013*a* Theory-based scaling of the SOL width in circular limited tokamak plasmas. *Nucl. Fusion* **53** (12), 122001.

HASEGAWA, A. & WAKATANI, M. 1983 Plasma edge turbulence. *Phys. Rev. Lett.* **50** (9), 682.

HINTON, F. L. 1991 Thermal confinement bifurcation and the L- to H-mode transition in tokamaks. *Phys. Fluids* B **3** (3), 696–704.

HONG, R., TYNAN, G. R., DIAMOND, P. H., NIE, L., GUO, D., LONG, T., KE, R., WU, Y., YUAN, B., XU, M., *et al.* 2017 Edge shear flows and particle transport near the density limit of the HL-2A tokamak. *Nucl. Fusion* **58** (1), 016041.

HORACEK, J., PITTS, R. A. & GRAVES, J. P. 2005 Overview of edge electrostatic turbulence experiments on TCV. *Czech. J. Phys.* **55** (3), 271–283.

JENKO, F. & DORLAND, W. 2001 Nonlinear electromagnetic gyrokinetic simulations of tokamak plasmas. *Plasma Phys. Control. Fusion* **43** (12A), A141.

JOLLIET, S., HALPERN, F. D., LOIZU, J., MOSETTO, A. & RICCI, P. 2014 Aspect ratio effects on limited scrape-off layer plasma turbulence. *Phys. Plasmas* **21** (2), 022303.

KAMADA, Y., HOSOGANE, N., YOSHINO, R., HIRAYAMA, T. & TSUNEMATSU, T. 1991 Study of the density limit with pellet fuelling in JT-60. *Nucl. Fusion* **31** (10), 1827.

KRIETE, D. M., MCKEE, G. R., SCHMITZ, L., SMITH, D. R., YAN, Z., MORTON, L. A. & FONCK, R. J. 2020 Effect of magnetic perturbations on turbulence-flow dynamics at the L–H transition on DIII-D. *Phys. Plasmas* **27** (6), 062507.

KU, S., CHANG, C. S., HAGER, R., CHURCHILL, R. M., TYNAN, G. R., CZIEGLER, I., GREENWALD, M., HUGHES, J., PARKER, S. E., ADAMS, M. F., *et al.* 2018 A fast low-to-high confinement mode bifurcation dynamics in the boundary-plasma gyrokinetic code XGC1. *Phys. Plasmas* **25** (5), 056107.

KUBE, R., GARCIA, O. E., THEODORSEN, A., BRUNNER, D., KUANG, A. Q., LABOMBARD, B. & TERRY, J. L. 2018 Intermittent electron density and temperature fluctuations and associated fluxes in the Alcator C-Mod scrape-off layer. *Plasma Phys. Control. Fusion* **60** (6), 065002.

LABOMBARD, B., BOIVIN, R. L., GREENWALD, M., HUGHES, J., LIPSCHULTZ, B., MOSESSIAN, D., PITCHER, C. S., TERRY, J. L., ZWEBEN, S. J. & ALCATOR GROUP. 2001 Particle transport in the scrape-off layer and its relationship to discharge density limit in Alcator C-Mod. *Phys. Plasmas* **8** (5), 2107–2117.

LABOMBARD, B., HUGHES, J. W., MOSESSIAN, D., GREENWALD, M., LIPSCHULTZ, B., TERRY, J. L. & THE ALCATOR C-MOD TEAM. 2005 Evidence for electromagnetic fluid drift turbulence controlling the edge plasma state in the Alcator C-Mod tokamak. *Nucl. Fusion* **45** (12), 1658.

LANG, P. T., SUTTROP, W., BELONOHY, E., BERNERT, M., MC DERMOTT, R. M., FISCHER, R., HOBIRK, J., KARDAUN, O. J. W. F., KOCSIS, G., KURZAN, B., *et al.* 2012 High-density H-mode operation by pellet injection and ELM mitigation with the new active in-vessel saddle coils in ASDEX Upgrade. *Nucl. Fusion* **52** (2), 023017.

LOIZU, J., RICCI, P., HALPERN, F. D. & JOLLIET, S. 2012 Boundary conditions for plasma fluid models at the magnetic presheath entrance. *Phys. Plasmas* **19** (12), 122307.

LOIZU, J., RICCI, P., HALPERN, F. D., JOLLIET, S. & MOSETTO, A. 2013 On the electrostatic potential in the scrape-off layer of magnetic confinement devices. *Plasma Phys. Control. Fusion* **55** (12), 124019.

MAGGI, C. F., WEISEN, H., HILLESHEIM, J. C., CHANKIN, A., DELABIE, E., HORVATH, L., AURIEMMA, F., CARVALHO, I. S., CORRIGAN, G., FLANAGAN, J., *et al.* 2017 Isotope effects on LH threshold and confinement in tokamak plasmas. *Plasma Phys. Control. Fusion* **60** (1), 014045.

MAHDAVI, M. A., OSBORNE, T. H., LEONARD, A. W., CHU, M.-S., DOYLE, E. J., FENSTERMACHER, M. E., MCKEE, G. R., STAEBLER, G. M., PETRIE, T. W., WADE, M. R., *et al.* 2002 High performance H mode plasmas at densities above the Greenwald limit. *Nucl. Fusion* **42** (1), 52.

MARTIN, Y., BEHN, R., FURNO, I., LABIT, B., REIMERDES, H. & THE TCV TEAM. 2014 H-mode access during plasma current ramp-up in TCV. *Nucl. Fusion* **54** (11), 114006.

MARTIN, Y. R., TAKIZUKA, T. & THE ITPA CDBM H-MODE THRESHOLD DATABASE WORKING GROUP. 2008 Power requirement for accessing the H-mode in ITER. *J. Phys.: Conf. Ser.* **123**, 012033.

MCDERMOTT, R. M., LIPSCHULTZ, B., HUGHES, J. W., CATTO, P. J., HUBBARD, A. E., HUTCHINSON, I. H., GRANETZ, R. S., GREENWALD, M., LABOMBARD, B., MARR, K., *et al.* 2009 Edge radial electric field structure and its connections to H-mode confinement in Alcator C-Mod plasmas. *Phys. Plasmas* **16** (5), 056103.

MERTENS, V., KAUFMANN, M., NEUHAUSER, J., SCHWEINZER, J., STOBER, J., BUCHL, K., GRUBER, O., HAAS, G., HERRMANN, A., KALLENBACH, A., *et al.* 1997 High density operation close to Greenwald limit and H mode limit in ASDEX upgrade. *Nucl. Fusion* **37** (11), 1607.

MOSETTO, A., HALPERN, F. D., JOLLIET, S., LOIZU, J. & RICCI, P. 2013 Turbulent regimes in the tokamak scrape-off layer. *Phys. Plasmas* **20** (9), 092308.

MOSETTO, A., HALPERN, F. D., JOLLIET, S., LOIZU, J. & RICCI, P. 2015 Finite ion temperature effects on scrape-off layer turbulence. *Phys. Plasmas* **22** (1), 012308.

MYRA, J. R., D'IPPOLITO, D. A., RUSSELL, D. A., UMANSKY, M. V. & BAVER, D. A. 2016 Analytical and numerical study of the transverse Kelvin–Helmholtz instability in tokamak edge plasmas. *J. Plasma Phys.* **82** (2), 905820210.

NESPOLI, F., FURNO, I., LABIT, B., RICCI, P., AVINO, F., HALPERN, F. D., MUSIL, F. & RIVA, F. 2017 Blob properties in full-turbulence simulations of the TCV scrape-off layer. *Plasma Phys. Control. Fusion* **59** (5), 055009.

NIELSEN, A. H., XU, G. S., MADSEN, J., NAULIN, V., JUUL RASMUSSEN, J. & WAN, B. N. 2015 Simulation of transition dynamics to high confinement in fusion plasmas. *Phys. Lett.* A **379** (47–48), 3097–3101.

OWEN, L. W., CARRERAS, B. A., MAINGI, R., MIODUSZEWSKI, P. K., CARLSTROM, T. N. & GROEBNER, R. J. 1998 Assessment of effects of neutrals on the power threshold for LH transitions in DIII-D. *Plasma Phys. Control. Fusion* **40** (5), 717.

PAN, Q., TOLD, D., SHI, E. L., HAMMETT, G. W. & JENKO, F. 2018 Full-f version of GENE for turbulence in open-field-line systems. *Phys. Plasmas* **25** (6), 062303.

PARUTA, P., BEADLE, C., RICCI, P. & THEILER, C. 2019 Blob velocity scaling in diverted tokamaks: a comparison between theory and simulation. *Phys. Plasmas* **26** (3), 032302.

PARUTA, P., RICCI, P., RIVA, F., WERSAL, C., BEADLE, C. & FREI, B. 2018 Simulation of plasma turbulence in the periphery of diverted tokamak by using the GBS code. *Phys. Plasmas* **25** (11), 112301.

QIN, H., COHEN, R. H., NEVINS, W. M. & XU, X. Q. 2007 Geometric gyrokinetic theory for edge plasmas. *Phys. Plasmas* **14** (5), 056110.

RASMUSSEN, J. J., NIELSEN, A. H., MADSEN, J., NAULIN, V. & XU, G. S. 2015 Numerical modeling of the transition from low to high confinement in magnetically confined plasma. *Plasma Phys. Control. Fusion* **58** (1), 014031.

REWOLDT, G., TANG, W. M., KAYE, S. & MENARD, J. 1996 Microinstability properties of small-aspect-ratio tokamaks. *Phys. Plasmas* **3** (5), 1667–1672.

RICCI, P., HALPERN, F. D., JOLLIET, S., LOIZU, J., MOSETTO, A., FASOLI, A., FURNO, I. & THEILER, C. 2012 Simulation of plasma turbulence in scrape-off layer conditions: the GBS code, simulation results and code validation. *Plasma Phys. Control. Fusion* **54** (12), 124047.

RICCI, P. & ROGERS, B. N. 2013 Plasma turbulence in the scrape-off layer of tokamak devices. *Phys. Plasmas* **20** (1), 010702.

RICCI, P., ROGERS, B. N. & BRUNNER, S. 2008 High- and low-confinement modes in simple magnetized toroidal plasmas. *Phys. Rev. Lett.* **100** (22), 6–9.

RIGHI, E., BARTLETT, D. V., CHRISTIANSEN, J. P., CONWAY, G. D., CORDEY, J. G., ERIKSSON, L.-G., DE ESCH, H. P. L., FISHPOOL, G. M., GOWERS, C. W., DE HAAS, J. C. M., *et al.* 1999 Isotope scaling of the H mode power threshold on JET. *Nucl. Fusion* **39** (3), 309.

RIVA, F., RICCI, P., HALPERN, F. D., JOLLIET, S., LOIZU, J. & MOSETTO, A. 2014 Verification methodology for plasma simulations and application to a scrape-off layer turbulence code. *Phys. Plasmas* **21** (6), 062301.

ROGERS, B. N. & DORLAND, W. 2005 Noncurvature-driven modes in a transport barrier. *Phys. Plasmas* **12** (6), 062511.

ROGERS, B. N., DRAKE, J. F. & ZEILER, A. 1998 Phase space of tokamak edge turbulence, the L–H transition, and the formation of the edge pedestal. *Phys. Rev. Lett.* **81** (20), 4396.

ROGERS, B. N. & RICCI, P. 2010 Low-frequency turbulence in a linear magnetized plasma. *Phys. Rev. Lett.* **104** (22), 225002.

ROSS, A., STEGMEIR, A., MANZ, P., GROSELJ, D., ZHOLOBENKO, W., COSTER, D. & JENKO, F. 2019 On the nature of blob propagation and generation in the large plasma device: global GRILLIX studies. *Phys. Plasmas* **26** (10), 102308.

RYTER, F., CAVEDON, M., HAPPEL, T., MCDERMOTT, R. M., VIEZZER, E., CONWAY, G. D., FISCHER, R., KURZAN, B., PÜTTERICH, T., TARDINI, G., *et al.* 2015 L–H transition physics in hydrogen and deuterium: key role of the edge radial electric field and ion heat flux. *Plasma Phys. Control. Fusion* **58** (1), 014007.

RYTER, F., ORTE, L. B., KURZAN, B., MCDERMOTT, R. M., TARDINI, G., VIEZZER, E., BERNERT, M., FISCHER, R. & THE ASDEX UPGRADE TEAM. 2014 Experimental evidence for the key role of the ion heat channel in the physics of the L–H transition. *Nucl. Fusion* **54** (8), 083003.

RYTER, F., RATHGEBER, S. K., ORTE, L. B., BERNERT, M., CONWAY, G. D., FISCHER, R., HAPPEL, T, KURZAN, B., MCDERMOTT, R. M., SCARABOSIO, A., *et al.* 2013 Survey of the H-mode power threshold and transition physics studies in ASDEX Upgrade. *Nucl. Fusion* **53** (11), 113003.

SAIBENE, G., HORTON, L. D., SARTORI, R., BALET, B., CLEMENT, S., CONWAY, G. D., CORDEY, J. G., DE ESCH, H. P. L., INGESSON, L. C., LINGERTAT, J., *et al.* 1999 The influence of isotope mass, edge magnetic shear and input power on high density ELMy H modes in JET. *Nucl. Fusion* **39** (9), 1133.

SCAGGION, A., MARTIN, Y., REIMERDES, H. & THE TCV TEAM. 2012 H-mode access with different X-point height in TCV. In *39th EPS Conference on Plasma Physics 2012, EPS 2012 and the 16th International Congress on Plasma Physics*.

SCHIRMER, J., CONWAY, G. D., ZOHM, H., SUTTROP, W. & THE ASDEX UPGRADE TEAM. 2006 The radial electric field and its associated shear in the ASDEX Upgrade tokamak. *Nucl. Fusion* **46** (9), S780.

SCHMID, B., MANZ, P., RAMISCH, M. & STROTH, U. 2017 Collisional scaling of the energy transfer in drift-wave zonal flow turbulence. *Phys. Rev. Lett.* **118** (5), 055001.

SCOTT, B. 1997 Three-dimensional computation of drift Alfvén turbulence. *Plasma Phys. Control. Fusion* **39** (10), 1635–1668.

SHAING, K. C. & HSU, C. T. 1995 Critical neutral density for high-mode bifurcation in tokamaks. *Phys. Plasmas* **2** (6), 1801–1803.

SHEIKH, U. A., DUNNE, M., FRASSINETTI, L., BLANCHARD, P., DUVAL, B. P., LABIT, B., MERLE, A., SAUTER, O., THEILER, C., TSUI, C. F., *et al.* 2018 Pedestal structure and energy confinement studies on TCV. *Plasma Phys. Control. Fusion* **61** (1), 014002.

SHI, E. L., HAMMETT, G. W., STOLTZFUS-DUECK, T. & HAKIM, A. 2017 Gyrokinetic continuum simulation of turbulence in a straight open-field-line plasma. *J. Plasma Phys.* **83** (3), 1–27.

SNIPES, J. A., BOIVIN, R. L., CHRISTENSEN, C., FIORE, C., GARNIER, D., GOETZ, J., GOLOVATO, S. N., GRAF, M., GRANETZ, R. S., GREENWALD, M., *et al.* 1996 Characteristics of high-confinement modes in Alcator C Mod. *Phys. Plasmas* **3** (5), 1992–1998.

SNYDER, P. B., GROEBNER, R. J., LEONARD, A. W., OSBORNE, T. H. & WILSON, H. R. 2009 Development and validation of a predictive model for the pedestal height. *Phys. Plasmas* **16** (5), 056118.

SNYDER, P. B., WILSON, H. R., FERRON, J. R., LAO, L. L., LEONARD, A. W., MOSSESSIAN, D., MURAKAMI, M., OSBORNE, T. H., TURNBULL, A. D. & XU, X. Q. 2004 ELMs and constraints on the H-mode pedestal: peeling–ballooning stability calculation and comparison with experiment. *Nucl. Fusion* **44** (2), 320.

STABLER, A., MCCORMICK, K., MERTENS, V., MULLER, E. R., NEUHAUSER, J., NIEDERMEYER, H., STEUER, K.-H., ZOHM, H., DOLLINGER, F., EBERHAGEN, A., *et al.* 1992 Density limit investigations on ASDEX. *Nucl. Fusion* **32** (9), 1557.

STANGEBY, P. C. 2000 *The Plasma Boundary of Magnetic Fusion Devices*. CRC.

STEGMEIR, A., COSTER, D., ROSS, A., MAJ, O., LACKNER, K. & POLI, E. 2018 GRILLIX: a 3D turbulence code based on the flux-coordinate independent approach. *Plasma Phys. Control. Fusion* **60** (3), 035005.

STEGMEIR, A., ROSS, A., BODY, T., FRANCISQUEZ, M., ZHOLOBENKO, W., COSTER, D., MAJ, O., MANZ, P., JENKO, F., ROGERS, B. N., *et al.* 2019 Global turbulence simulations of the tokamak edge region with GRILLIX. *Phys. Plasmas* **26** (5), 052517.

STOLTZFUS-DUECK, T. 2012 Transport-driven toroidal rotation in the tokamak edge. *Phys. Rev. Lett.* **108** (6), 065002.

TAMAIN, P., BUFFERAND, H., CIRAOLO, G., COLIN, C., GALASSI, D., GHENDRIH, P., SCHWANDER, F. & SERRE, E. 2016 The TOKAM3X code for edge turbulence fluid simulations of tokamak plasmas in versatile magnetic geometries. *J. Comput. Phys.* **321**, 606–623.

TANAKA, H., OHNO, N., ASAKURA, N., TSUJI, Y., KAWASHIMA, H., TAKAMURA, S., UESUGI, Y. & THE JT-60U TEAM. 2009 Statistical analysis of fluctuation characteristics at high-and low-field sides in L-mode SOL plasmas of JT-60U. *Nucl. Fusion* **49** (6), 065017.

TERRY, P. W. 2000 Suppression of turbulence and transport by sheared flow. *Rev. Mod. Phys.* **72** (1), 109.

TERRY, J. L., ZWEBEN, S. J., HALLATSCHEK, K., LABOMBARD, B., MAQUEDA, R. J., BAI, B., BOSWELL, C. J., GREENWALD, M., KOPON, D., NEVINS, W. M., *et al.* 2003 Observations of the turbulence in the scrape-off-layer of Alcator C-Mod and comparisons with simulation. *Phys. Plasmas* **10** (5), 1739–1747.

THOMAS, D. M., GROEBNER, R. J., BURRELL, K. H., OSBORNE, T. H. & CARLSTROM, T. N. 1998 The back transition and hysteresis effects in DIII-D. *Plasma Phys. Control. Fusion* **40** (5), 707.

VALOVIC, M., RAPP, J., CORDEY, J. G., BUDNY, R., MCDONALD, D. C., GARZOTTI, L., KALLENBACH, A., MAHDAVI, M. A., ONGENA, J., PARAIL, V., *et al.* 2002 Long timescale density peaking in JET. *Plasma Phys. Control. Fusion* **44** (9), 1911.

VERSHKOV, V. A. & MIRNOV, S. V. 1974 Role of impurities in current tokamak experiments. *Nucl. Fusion* **14** (3), 383.

VIEZZER, E., PÜTTERICH, T., ANGIONI, C., BERGMANN, A., DUX, R., FABLE, E., McDermott, R. M., Stroth, U., Wolfrum, E., *et al.* 2013 Evidence for the neoclassical nature of the radial electric field in the edge transport barrier of ASDEX Upgrade. *Nucl. Fusion* **54** (1), 012003.

WAGNER, F., BECKER, G., BEHRINGER, K., CAMPBELL, D., EBERHAGEN, A., ENGELHARDT, W., FUSSMANN, G., GEHRE, O., GERNHARDT, J., GIERKE, G. V., *et al.* 1982 Regime of improved confinement and high beta in neutral-beam-heated divertor discharges of the ASDEX tokamak. *Phys. Rev. Lett.* **49** (19), 1408.

WAN, W., PARKER, S. E., CHEN, Y., GROEBNER, R. J., YAN, Z., PANKIN, A. Y. & KRUGER, S. E. 2013 Global gyrokinetic simulations of the H-mode tokamak edge pedestal. *Phys. Plasmas* **20** (5), 055902.

WERSAL, C. & RICCI, P. 2015 A first-principles self-consistent model of plasma turbulence and kinetic neutral dynamics in the tokamak scrape-off layer. *Nucl. Fusion* **55** (12), 123014.

WIESENBERGER, M., EINKEMMER, L., HELD, M., GUTIERREZ-MILLA, A., SAEZ, X. & IAKYMCHUK, R. 2019 Reproducibility, accuracy and performance of the feltor code and library on parallel computer architectures. *Comput. Phys. Commun.* **238**, 145–156.

XU, X. Q., COHEN, R. H., NEVINS, W. M., PORTER, G. D., RENSINK, M. E., ROGNLIEN, T. D., MYRA, J. R., D'IPPOLITO, D. A., MOYER, R. A., SNYDER, P. B., *et al.* 2002 Turbulence simulations of X point physics in the LH transition. *Nucl. Fusion* **42** (1), 21.

XU, X. Q., COHEN, R. H., ROGNLIEN, T. D. & MYRA, J. R. 2000 Low-to-high confinement transition simulations in divertor geometry. *Phys. Plasmas* **7** (5), 1951–1958.

YU, G. Q., KRASHENINNIKOV, S. I. & GUZDAR, P. N. 2006 Two-dimensional modelling of blob dynamics in tokamak edge plasmas. *Phys. Plasmas* **13** (4), 042508.

YUSHMANOV, P. N., TAKIZUKA, T., RIEDEL, K. S., KARDAUN, O. J. W. F., CORDEY, J. G., KAYE, S. M. & POST, D. E. 1990 Scalings for tokamak energy confinement. *Nucl. Fusion* **30** (10), 1999.

ZEILER, A., DRAKE, J. F. & ROGERS, B. 1997 Nonlinear reduced Braginskii equations with ion thermal dynamics in toroidal plasma. *Phys. Plasmas* **4** (6), 2134–2138.

ZHU, B., FRANCISQUEZ, M. & ROGERS, B. N. 2017 Global 3D two-fluid simulations of the tokamak edge region: turbulence, transport, profile evolution, and spontaneous E × B rotation. *Phys. Plasmas* **24** (5), 055903.

ZHU, B., FRANCISQUEZ, M. & ROGERS, B. N. 2018 GDB: a global 3D two-fluid model of plasma turbulence and transport in the tokamak edge. *Comput. Phys. Commun.* **232**, 46–58.